Nicotine up-regulates α4β2 nicotinic receptors and ER exit sites via stoichiometry-dependent chaperoning

Rahul Srinivasan, Rigo Pantoja, Fraser J. Moss, Elisha D.W. Mackey, Cagdas D. Son, Julie Miwa, and Henry A. Lester

Division of Biology MC 156-29, California Institute of Technology, Pasadena, CA 91125

The up-regulation of α4β2* nicotinic acetylcholine receptors (nAChRs) by chronic nicotine is a cell-delimited process and may be necessary and sufficient for the initial events of nicotine dependence. Clinical literature documents an inverse relationship between a person's history of tobacco use and his or her susceptibility to Parkinson's disease; this may also result from up-regulation. This study visualizes and quantifies the subcellular mechanisms involved in nicotine-induced nAChR up-regulation by using transfected fluorescent protein (FP)-tagged α4 nAChR subunits and an FP-tagged Sec24D endoplasmic reticulum (ER) exit site marker. Total internal reflection fluorescence microscopy shows that nicotine (0.1 µM for 48 h) up-regulates α4β2 nAChRs at the plasma membrane (PM), despite increasing the fraction of α4β2 nAChRs that remain in near-PM ER. Pixel-resolved normalized Förster resonance energy transfer microscopy between α4-FP subunits shows that nicotine stabilizes the $(\alpha 4)_2(\beta 2)_3$ stoichiometry before the nAChRs reach the trans-Golgi apparatus. Nicotine also induces the formation of additional ER exit sites (ERES). To aid in the mechanistic analysis of these phenomena, we generated a $\beta 2_{enhanced-ER-export}$ mutant subunit that mimics two regions of the β4 subunit sequence: the presence of an ER export motif and the absence of an ER retention/retrieval motif. The $\alpha 4\beta 2_{enhanced-ER-export}$ nAChR resembles nicotine-exposed nAChRs with regard to stoichiometry, intracellular mobility, ERES enhancement, and PM localization. Nicotine produces only small additional PM up-regulation of $\alpha 4\beta 2_{enhanced-ER-export}$ receptors. The experimental data are simulated with a model incorporating two mechanisms: (1) nicotine acts as a stabilizing pharmacological chaperone for nascent α4β2 nAChRs in the ER, eventually increasing PM receptors despite a bottleneck(s) in ER export; and (2) removal of the bottleneck (e.g., by expression of the $\beta 2_{enhanced-ER-export}$ subunit) is sufficient to increase PM nAChR numbers, even without nicotine. The data also suggest that pharmacological chaperoning of nAChRs by nicotine can alter the physiology of ER processes.

INTRODUCTION

Repeated or chronic exposure to nicotine—beyond the seconds and minutes that lead to receptor activation and/or desensitization—is essential for nicotine dependence (Kauer and Malenka, 2007; Kalivas et al., 2009; Koob, 2009). Chronic exposure also apparently underlies the inverse correlation between a person's history of tobacco use and his or her susceptibility to Parkinson's disease (Ritz et al., 2007). Literature since 1983 also shows that chronic nicotine increases the number of neuronal nicotinic acetylcholine receptors (nAChRs) (Marks et al., 1983; Schwartz and Kellar, 1983). nAChRs, a superfamily of ligand-gated ion channels, activated by acetylcholine and nicotine, assemble as homopentameric or heteropentameric complexes comprising various combinations of α (α2 to α10) and β (β2 to β4) subunits (Gotti et al., 2006).

Nicotine-induced "up-regulation" has been replicated many times in systems ranging from clonal cell lines to primary neurons in culture, to mouse models, and to smokers' brains (Breese et al., 1997; Court et al., 1998; Staley et al., 2006; Mukhin et al., 2008; Albuquerque et al., 2009; Lester et al., 2009). Bronchial epithelium cells also express nAChRs, and these are also up-regulated by nicotine (Fu et al., 2009). One or more mechanisms common to all such cellular systems presumably govern up-regulation. Therefore, studies with mechanistically favorable heterologously expressed preparations, such as nAChRs in oocytes and clonal mammalian cell lines, have good relevance to the pathophysiology of chronic nicotine. Data from such favorable systems show that nicotine enhances the assembly of functional nAChRs containing the α4 and β2 subunits and also causes the preferential assembly of receptors with $(\alpha 4)_2(\beta 2)_3$

stoichiometry (Buisson and Bertrand, 2001; Nelson et al., 2003; Kuryatov et al., 2005; Sallette et al., 2005; Vallejo et al., 2005; Son et al., 2009).

Mechanisms proposed for the effect of nicotine on nAChR assembly include the idea that nicotine acts as a maturational enhancer (Sallette et al., 2005), a novel slow stabilizer (Vallejo et al., 2005), and/or a pharmacological chaperone of nAChRs (Kuryatov et al., 2005; Lester et al., 2009). Although the studies cited derived mainly from experiments on clonal cell lines, this hypothesis becomes more attractive in view of electron microscopy studies in mouse dorsal raphe and rat cortical neurons, showing that endogenous α4β2 nAChRs localize at least partially to the smooth ER (Hill et al., 1993; Commons, 2008).

Nicotine may also affect the rate of receptor turnover by decreasing the lysosomal degradation of nAChRs at the cell periphery (Peng et al., 1994). Alternative models propose that the binding of nicotine to surface receptors can trigger up-regulation (Whiteaker et al., 1998), that up-regulation can be initiated by the desensitization of surface nAChRs (Fenster et al., 1999), and that up-regulation requires exocytosis machinery (Darsow et al., 2005).

Other important mechanistic facts come from observations that nAChRs are also up-regulated by antagonists (Gopalakrishnan et al., 1996), and that drug–receptor binding plays a major role in up-regulation (Kishi and Steinbach, 2006). Moreover, nAChR mRNA levels remain constant after nicotine exposure (Marks et al., 1992; Peng et al., 1994; Ke et al., 1998). These data argue against roles for Ca^{2+}-induced second messenger signaling cascades and transcriptional processes in nicotine-induced nAChR up-regulation. Vital information on several aspects of up-regulation has thus been obtained.

In the spirit of obtaining rigorous mechanistic data on the phenomenon of up-regulation, which occurs in a broad range of heterologous and endogenous expression systems, this study exploits a cellular system that has favorable optical characteristics and offers excellent control of expressed protein levels. We use a combination of live cell, subcellularly resolved total internal reflection fluorescence (TIRF) microscopy, confocal microscopy, and Förster resonance energy transfer (FRET) analysis to assess the effects of nicotine on the assembly, ER exit, and plasma membrane (PM) insertion of heterologously expressed, fluorescently tagged α4β2 nAChRs. Furthermore, we identify novel motifs governing the ER localization of α4β2 nAChRs within the β2 subunit M3–M4 large intracellular loop and show that these motifs modulate the stoichiometry and ER exit of α4β2 nAChRs.

It is also important to understand whether up-regulation has consequences for other aspects of cell physiology, such as exit from the ER. To this end, we use fluorescent Sec24D, a component of ER exit sites

(ERES). The data strongly support the following mechanism: the $(α4)_2(β2)_3$ stoichiometry would languish in the ER, but nicotine acts as a pharmacological chaperone to stabilize $(α4)_2(β2)_3$ nAChRs and presumably, as a consequence, ERES. The result: nAChRs reach the PM in greater numbers.

MATERIALS AND METHODS

Materials and reagents
PfuTurbo Cx Hotstart polymerase and the QuikChange II XL site-directed mutagenesis kit were purchased from Agilent Technologies. Mouse Neuro-2a cells (CCL-131) were obtained from American Type Culture Collection. Dulbecco's modified Eagle's medium (DMEM) with 4 mM L-glutamine, OptiMEM 1, Leibovitz L-15 imaging medium, ER-Tracker Green, and FBS were purchased from Invitrogen. Expressfect transfection reagent was purchased from Denville Scientific. Tissue culture flasks and plasticware were from Greiner Bio-One. Poly-D-lysine–coated 35-mm glass-bottom imaging dishes (1.5-mm coverslip thickness) were obtained from MatTek Corporation, and nicotine was purchased from Sigma-Aldrich.

Plasmid constructs
Mouse wild-type (wt) α4, β2, and β4 constructs were obtained from J. Stitzel (University of Colorado, Boulder, CO). Mouse α4-eGFP was engineered as described previously (Nashmi et al., 2003). In brief, eGFP was introduced in frame into the α4 BstEII site with an upstream HA tag after residue 426 in the M3–M4 intracellular loop. eGFP was PCR amplified from the peGFPN1 vector using the forward primer 5′-TTTTGGTCACCCTATCCT-TATGACGTCCCAGACTACGCCATGGTGAGCAAGGGCGAGG-AGCTG-3′ and the reverse primer 5′-AAAAGGCGTAGTCTG-GGACGTCATAAGGATAGGTGACCTCTTGTACAGCTCGTCCAT-GCCGAG-3′. The PCR product was cut with BstEII and ligated into the wt α4 construct to create α4-eGFP. Because mcherry contains BstEII sites, α4-mcherry was cloned without the use of standard restriction digestion and ligation reactions (Moss et al., 2009): mcherry was PCR amplified from the pCS2-mcherry plasmid using proofreading Pfu-Turbo Cx Hotstart polymerase and primers with 20–25 nucleotide 5′ and 3′ overhangs that were homologous to the mouse α4wt coding sequence. The PCR product was extracted and used as a primer in a second PCR step with QuikChange II XL site-directed mutagenesis kit to create the final α4-mcherry construct. Mutations were introduced into the α4-eGFP and β2wt constructs using the appropriate primers and QuikChange II XL site-directed mutagenesis kit to create the α4L358A-eGFP, β2-L349M, β2-365AAQA368, and the β2 double-mutant 365AAQA368 L349M constructs. PM reporter pCS2-mcherry was obtained from S. Fraser (California Institute of Technology, Pasadena, CA). The Sec24D-eYFP plasmid was provided by D.J. Stephens (University of Bristol School of Medical Sciences, Bristol, England, UK) (Stephens et al., 2000), and the GalT-eCFP plasmid was obtained from Addgene (plasmid 11931) (Cole et al., 1996). Sec24D-mcherry and Sec24D-eGFP were cloned from Sec24D-eYFP using the PCR integration method described above.

Cell culture and transfections
Mouse Neuro-2a cells were cultured using standard tissue culture techniques and maintained in DMEM plus 10% FBS (Son et al., 2009). Plasmid concentrations used for transfection were as follows: 500 ng of each nAChR and glutamate-gated chloride ion channel (GluCl) subunit, 75 ng pCS2-mcherry, 250 ng Sec24D construct, and 250 ng GalT-eCFP. 90,000 cells were plated in

poly-D-lysine–coated 35-mm glass-bottom imaging dishes (MatTek Corporation). The next day, plasmid DNA was mixed with cationic lipids by adding the appropriate DNA concentrations to 4 µl of Expressfect transfection reagent in 200 µl DMEM (final volume) and incubated for 20 min at room temperature to form cationic lipid–DNA complexes. DMEM plus DNA–lipid complexes were added to Neuro-2a cells in 1 ml DMEM plus 10% FBS and incubated at 37°C for 4 h. Dishes were rinsed twice with DMEM and then filled with 3 ml DMEM plus 10% FBS and incubated at 37°C for 48 h. For nicotine treatments, a concentration of 0.1 µM was used for 48 h because this is within the range of steady-state nicotine concentrations achieved in smokers' brains. Nicotine was added during media change after transfection.

TIRF microscopy (TIRFM)

Neuro-2a cells cultured in glass-bottom poly-D-lysine–coated imaging dishes (MatTek Corporation) were transfected with the appropriate plasmids and imaged live 48 h after transfection at 37°C in a stage-mounted culture dish incubator (Warner Instruments). TIRFM enables the visualization of fluorescently labeled intracellular molecules within ∼300 nm of the cell–coverslip interface (Oancea et al., 2006; Fish, 2009; Khiroug et al., 2009). TIRF images were obtained using an inverted microscope (IX71; Olympus) equipped with an Olympus PlanApo 100× 1.45 numerical aperture oil objective and a Mitutoyo micrometer to control the position of the fiber optic and TIRF evanescent field illumination. eGFP and mcherry fluorophores were excited with a 488-nm air-cooled argon laser (P/N IMA101040ALS; Melles Griot), and an Optosplit II image splitter (Cairn Research) was used to simultaneously detect fluorescence emission from eGFP and mcherry. Images were captured with either a 16-bit resolution EMCCD camera (Cascade; Photometrics; Figs. 1 and 3, and Videos 1 and 2) or an iXON DU-897 back-illuminated EMCCD camera (Figs. 2, 4, and 5, and Videos 3–5). Sample exposure rate, percent laser transmission, and gain parameters were initially adjusted and then maintained constant across all samples for each imaging session. 488- and 561-nm laser lines were linearly s-polarized as revealed using an achromatic 400–800-nm half-wave plate (AQWP05M-600; Thorlabs; provided by L. Wade, California Institute of Technology, Pasadena, CA).

To verify that TIRF can be used to simultaneously visualize the PM and peripheral ER, Neuro-2a cells were transfected with a PM reporter, pCS2-mcherry. At 48 h after transfection, cells were stained with 1 µM of BODIPY-tagged glibenclamide (ER-Tracker Green) and imaged within 2 min. BODIPY and mcherry fluorophores were excited with a 488-nm laser, and images of cellular footprints were simultaneously captured at red- and green-emission wavelengths. PM-localized pCS2-mcherry fluorescence was detected as a cellular footprint with uniform fluorescence, whereas ER-Tracker Green exhibited a reticulate pattern (Fig. 1 A, first and third columns). Merged images showed that the ER fluorescence was readily distinguishable from PM-localized mcherry (Fig. 1 A, first column).

To determine subcellular localization patterns of α4β2 and α4β4 nAChRs, Neuro-2a cells were transfected with either α4eGFP plus β2wt or with α4eGFP plus β4wt subunits and imaged at 48 h after transfection. In some experiments, pCS2-mcherry was included in the transfections to visualize the PM (Fig. 1 A, first, second, and fourth columns). α4-eGFP plus β2wt–transfected cells demonstrated reticulate eGFP labeling that resembled ER (Fig. 1 A, compare the first and second columns). To prove this point, we cotransfected cells with α4-mcherry plus β2wt and then stained them with ER-Tracker Green; the red and green fluorescence colocalized nearly completely (Fig. 1 A, third column). The ER fluorescence in α4eGFP plus β2wt–transfected cells was two- to threefold brighter than PM and displayed little to no vesicular dynamics (Video 1). In contrast, α4eGFP plus β4wt–transfected cells

showed much less reticulate fluorescence, but these cells also displayed vesicles within the TIRF footprint (Video 2). Vesicles were pleomorphic, with diameters ranging from 0.5 to 1 µm. Some vesicles appeared as elongated structures ranging from 2 to 5 µM in length. Vesicles were either stationary or showed spatial displacements of 0.5–5 µm/s within the TIRF footprint.

We quantified these apparently different localization patterns between α4eGFP plus β2wt and α4eGFP plus β4wt by separately measuring the intensity and extent of PM and ER fluorescence, as described in the next subsection, allowing us to unambiguously isolate nAChRs localized within the cellular PM (Fig. 1 B, 1 and 2). In all cases, we used the α4eGFP labeling to threshold, demarcate, and quantify PM- and ER-localized nAChRs. We found that α4eGFP plus β4wt–transfected cells showed a 1.9-fold increase in the PM-integrated density when compared with α4eGFP plus β2wt–transfected cells (Fig. 1 B, 3).

To quantify the fraction of ER fluorescence, we measured ratios of integrated densities (see next subsection) for the whole TIRF footprint to ER-localized signals (footprint/ER ratio). As an alternative analysis, we also generated simple frequency plots of fluorescence intensity versus number of pixels for either ER or whole footprint TIRF images. We observed that the ER pixel count showed an approximate twofold reduction for α4eGFP plus β4wt compared with α4eGFP plus β2wt–transfected cells (Fig. 1 D, 1 and 2). Measured ratios revealed an approximately threefold increase in ER-localized nAChRs for α4eGFP plus β2wt (footprint/ER ratio = 1.69) when compared with α4eGFP plus β4wt–transfected cells (footprint/ER ratio = 5.01; Fig. 1 D, 3). Collectively, these data provide evidence that α4β2 nAChRs primarily localize to the ER, and that β subunits partially control the subcellular localization and trafficking of α4β2 and α4β4 nAChRs, explaining many previous studies in which α4β4 nAChRs show better surface expression than α4β2.

Quantification of TIRF images (Figs. 1–4)

A comparison of α4eGFPβ2wt nAChR localization with the BODIPY-tagged glibenclamide (ER-Tracker Green) image showed that the fluorescence intensity of ER-localized nAChRs was always two- to threefold brighter than other regions of the TIRF footprint. Using ImageJ in pixel-by-pixel mode, we exploited this feature to selectively threshold and isolate either the ER or PM within raw images. The α4eGFP subunit served as a subcellular marker of nAChR localization. ER regions of interest (ROI) were demarcated as follows. We subtracted the average PM fluorescence intensity and background signal from the entire TIRF image. ER-localized nAChRs were then thresholded and demarcated (Fig. 1 B). PM fluorescence was extracted as follows. Raw TIRF images were converted to background-subtracted images, and the ER fluorescence was thresholded and masked. ER masks were subtracted from the original image to generate images with PM fluorescence signals (Fig. 1 C).

These procedures yielded a dataset of several hundred thousand pixel intensities over the 15–50 cells in each experimental group. Integrated densities are simply the sum of pixel values for either the PM or the ER or the ER plus PM (using whole TIRF footprint images). Mean PM-integrated densities were derived by dividing the total integrated density for each experimental group by the number of imaged cells and were used to measure the population of PM-localized receptors. Ratios of integrated densities for the whole TIRF footprint (ER plus PM) to ER were used to determine the post-Golgi fraction of receptors. Error bars for ratio plots were obtained by Pythagorean addition (also called addition in quadrature) of the relative standard errors for the numerator and denominator (see http://reference.wolfram.com/applications/eda/ExperimentalErrorsAndErrorAnalysis.html). For PM-integrated density measurements, rather than plotting SEMs (which would be indistinguishably small on the plots), we have used

"error bars" to depict 99% confidence intervals based on a two-tailed t test. Two ER fluorescence peaks are observed in Fig. 1 D (1). Because the ER displays a stacked tubular geometry, TIRF evanescent waves excite nAChRs localized at the PM as well as receptors located in the ER at increasing z distances from the cytoplasmic surface of the PM. Fluorescent signals from relatively distant ER-localized receptors thus lead to a subset of pixels with low fluorescence intensity, whereas ER-localized pixels that are closer to the PM appear bright.

Confocal imaging

An Eclipse C1si laser-scanning confocal microscope equipped with a 63× 1.4 numerical aperture VC Plan Apo oil objective and a 32-anode photomultiplier tube (Nikon) was used for confocal imaging. Before imaging, cell culture media was replaced with phenol red–free CO_2-independent Leibovitz L-15 medium. All experiments were performed in live cells 48 h after transfection at 37°C in a stage-mounted culture dish incubator (Warner Instruments). Cellular eCFP, eGFP, and mcherry fluorescence signals were acquired from 30–40 cells per dish after sequential excitation at 439- (for eCFP), 488- (for eGFP), and 561-nm (for mcherry) laser lines. Full-emission spectra were acquired in 5-nm bins between 470 and 620 nm, and the signal of each expressed fluorophore was linearly unmixed from the raw spectral image using reference spectra from control cells expressing solely the eCFP, eGFP, or mcherry fusion constructs.
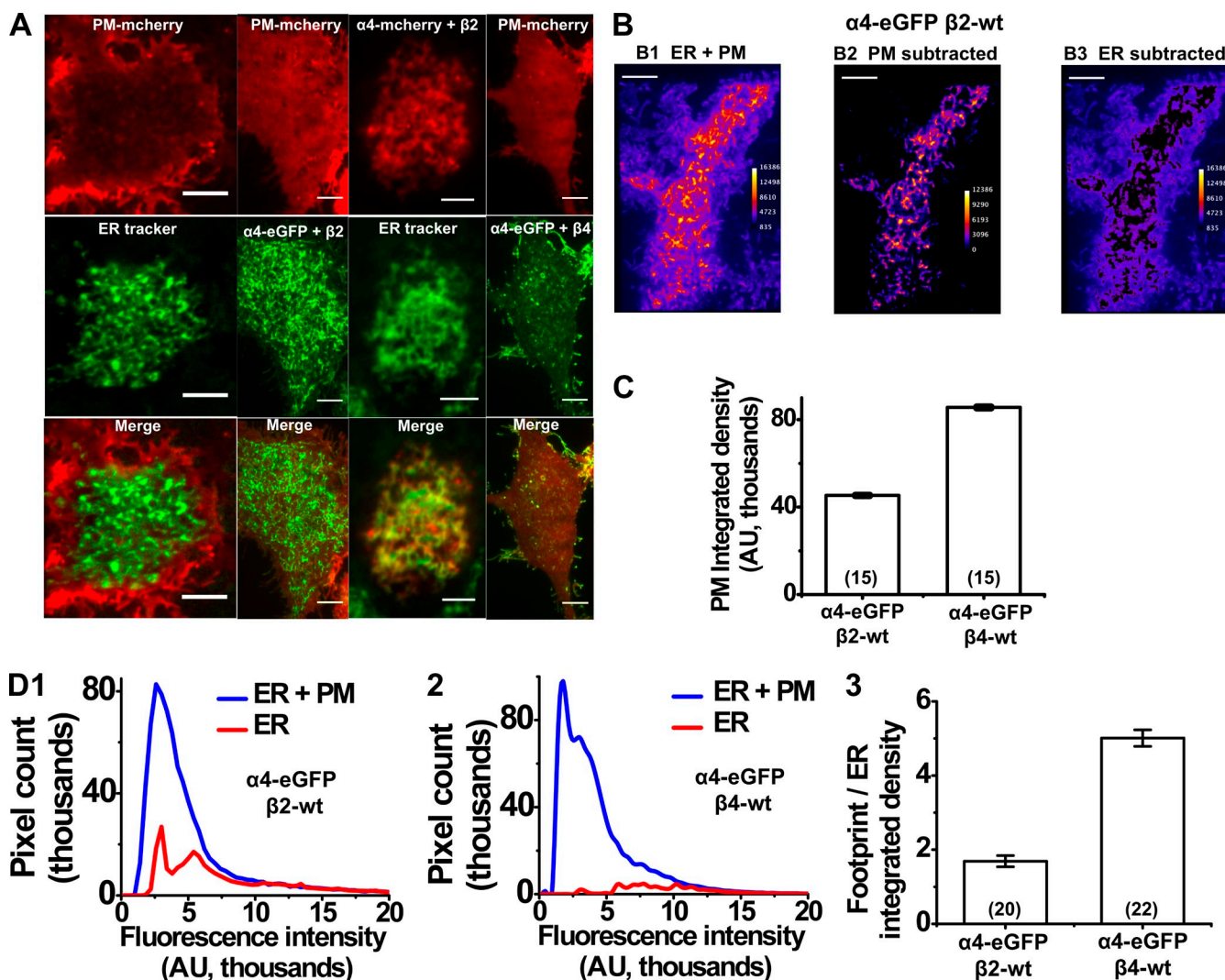
Figure 1. Subcellular localization of α4β2 and α4β4 nAChRs depends on the β subunit. (A) Representative TIRF images of Neuro-2a cells expressing a PM reporter (PM mcherry) or α4-mcherry plus β2wt along with either ER-Tracker Green or α4eGFP plus β2wt or α4eGFP plus β4wt. Each column is a different cell. Red and green fluorescence channels are separately shown in the top two rows, and merged images are in the bottom row. Panel labels indicate the fluorophore and transfected proteins. B1, pseudo-colored TIRF image of α4eGFP plus β2wt–transfected cell; B2, ER fluorescence signal from cell in B1 after subtraction of PM fluorescence; B3, PM fluorescence signal from cell in B1 after subtraction of ER fluorescence. (C) PM-integrated density for α4eGFP plus β2wt– and α4eGFP plus β4wt–transfected cells. Error bars show 99% confidence intervals. (D; 1 and 2) Plots showing number of pixels (y axis) versus fluorescence intensity (x axis) for either whole TIRF footprint (ER + PM) or the ER in α4eGFP plus β2wt– and α4eGFP plus β4wt–transfected cells. 3, the integrated density ratios of whole TIRF footprint to ER for α4eGFP plus β2wt and α4eGFP plus β4wt. Error bars are SEM. Number of imaged cells are indicated in parentheses. Bars, 5 µm.

Pixel-by-pixel normalized FRET (NFRET) from sensitized acceptor emission

The theory and analysis for FRET measurements of oligomeric protein complexes and nAChR stoichiometry have been described previously (Drenan et al., 2008; Moss et al., 2009; Son et al., 2009). For NFRET experiments, Neuro-2a cells were transfected with GalT-eCFP plus α4-eGFP plus α4-mcherry plus wt or mutant β2 subunits. GalT-eCFP was used to label the trans-Golgi/trans-Golgi network (TG/TGN) (Schaub et al., 2006). Cells transfected with either α4-eGFPβ2wt or α4-mcherryβ2wt were included in every imaging session to control for pixel saturation and spectral bleedthrough (BT).

Live cells were imaged using an Eclipse C1si laser-scanning confocal microscope. During image acquisition, cells were focused to a plane where the GalT-eCFP fluorescence was best visualized. Images with emission spectra for eCFP, eGFP, and mcherry were acquired in 5-nm bins between 470 and 620 nm. 439-, 488-, and 561-nm laser lines were used to excite eCFP, eGFP, and mcherry, respectively. Images were linearly unmixed using reference spectra for eCFP, eGFP, and mcherry with emission maxima at 477, 508, and 608 nm. Reference spectra were acquired from Neuro-2a cells transfected with either GalT-eCFP or α4-eGFPβ2wt or α4-mcherryβ2wt during the same imaging session. Linear unmixing was used to separate all three emission spectra from each image. Linearly unmixed images were compiled into donor BT stacks, acceptor BT stacks, and sample image stacks.

The PixFRET ImageJ plug-in was used to determine the eGFP and mcherry BT values and to calculate the net FRET (nF) (Eq. 1) and NFRET at each pixel (Feige et al., 2005). With the background and BT corrections set, the nF for each pixel as described by Eq. 1 was calculated, and the data were presented as 32-bit images. nF was divided by the square root of eGFP and mcherry intensities (Eq. 2) to obtain the NFRET value at each pixel. FRET normalization was used to control for large differences in fluorophore expression within subcellular regions and between different cells in a dish.

$$nF = I_{FRET} - I_{eGFP} \times BT_{eGFP} - I_{mcherry} \times BT_{mcherry} \qquad (1)$$

$$NFRET = \frac{I_{FRET} - I_{eGFP} \times BT_{eGFP} - I_{mcherry} \times BT_{mcherry}}{\sqrt{I_{eGFP} \times I_{mcherry}}}, \qquad (2)$$

where I_{FRET} = mcherry-sensitized emission with 488-nm excitation, I_{eGFP} = eGFP emission with 488-nm excitation, BT_{eGFP} = BT of eGFP emission into mcherry emission spectra at 488-nm excitation, $I_{mcherry}$ = mcherry emission with 561-nm excitation, and $BT_{mcherry}$ = BT of mcherry emission into eGFP emission spectra at 561-nm excitation. I_{FRET}, I_{eGFP}, and $I_{mcherry}$ were obtained from Neuro-2a cells transfected with GalT-eCFP plus α4-eGFP plus α4-mcherry plus wt β2. BT_{eGFP} and $BT_{mcherry}$ values were obtained from Neuro-2a cells transfected with α4-eGFP plus β2wt and α4-mcherry plus β2wt, respectively.

Histograms of NFRET (x axis) versus number of pixels (y axis) of each imaged cell were compiled for either the whole cell sections or the TG/TGN ROI, demarcated by intensity-based thresholding of GalT-eCFP fluorescence. Frequency histograms obtained in this way (omitting values of zero) were merged for all cells in each experimental group and fitted to Gaussian components. Ratios of area under the curve for Gaussian components with high and low mean NFRET values were used to determine changes in receptor stoichiometry between experimental groups.

ERES quantification

Neuro-2a cells were cotransfected with the appropriate nAChR/GluCl subunits and the ERES marker, Sec24D-mcherry. Each cell was focused to a plane where the maximum ERES were visualized. Sequential images of eGFP and mcherry fluorescence were obtained and linearly unmixed. For quantification, ERES ROI were demarcated using intensity-based thresholding and counted for each cell using the particle analysis feature in ImageJ (version 1.44 or later; Abramoff et al., 2004). Error bars for ERES measurements are ± SEM, and p-values are based on a two-tailed *t* test.

Simulation of the SePhaChARNS 2.0 model

The selective pharmacological chaperoning of acetylcholine receptor number and stoichiometry (SePhaChARNS) 2.0 model (Fig. 7) was constructed to simulate six experimentally observed "target measures" that arise from the fluorescence data. The target measures are defined fully in Results. We used MATLAB R2010a (SimBio Toolbox; The MathWorks, Inc.) and saved the model as a file with the .sbproj extension. We defined a normalized residual for each of the simulated values: residual = [(simulated value − target measure)/target measure]. The objective function to be optimized was the summed squares of the six residuals (see Results), and we sought parameters that reduced the objective function to <0.01. Thus, no residual exceeded 10%, and the average residual was 4%. The parameters were optimized using the MATLAB Global Optimization toolbox, Genetic Algorithm (this provided more efficient optimization than the simulating annealing algorithm). Typical optimizations of nine parameters required 10^5–10^6 simulations (<1 h on a 2-Ghz processor with compiled code).

Other data analyses

Protein sequence alignments were done with DNASTAR software (Lasergene version 8.1).

Online supplemental material

The supplemental material consists of five TIRFM videos of Neuro-2a cells and is available at http://www.jgp.org/cgi/content/full/jgp.201010532/DC1.

RESULTS

## α4β2 nAChR up-regulation monitored optically

Fig. 2 presents data on nicotine-induced up-regulation in an optical assay based on TIRFM (see Materials and methods; Fig. 1). Representative TIRF images and the optical analyses are shown in Fig. 2 A. PM-localized α4β2 nAChRs are quantified in Fig. 2 B. The PM up-regulation of wt nAChRs by nicotine, which amounts to 1.9-fold, recapitulates many experiments cited in the Introduction in various systems. The experiments use a nicotine concentration (0.1 µM) somewhat less than that in the blood within a few min after a human smokes a cigarette, and perhaps more appropriate to the average values during a day of smoking (Matta et al., 2007). The time scale is also relevant to the initial stages of nicotine-induced up-regulation in the brains of mice (Marks et al., 1985).

Fig. 2 A compares nAChRs in near-PM ER versus that in the whole TIRF footprint (see Materials and methods; Fig. 1). Interestingly, Fig. 2 C shows that despite the nicotine-induced up-regulation at the PM, up-regulation is also associated with a notable relative decrease in the ratio of whole TIRF footprint to ER-resident wt nAChRs.

In control solutions, the footprint/ER ratio was 3.42; nicotine treatment reduced the footprint/ER ratio to 2.19. Evidently, up-regulation takes place despite an overall bias toward ER-resident nAChRs.

Fig. 2 A also shows that the pattern of up-regulation differs between α4β2 nAChRs and those in which the α4 subunit is coexpressed with a so-called β2$_{enhanced-ER-export}$ double-mutant subunit. The α4β2$_{enhanced-ER-export}$ nAChRs

localize strongly to the PM, even in the absence of nicotine; nicotine produces only a modest further up-regulation at the PM. We chose to mutate the β2 subunit because the TIRF experiments presented in Materials and methods (Fig. 1) showed dramatic differences in the subcellular localization and the intracellular mobility of α4β2 versus α4β4 nAChRs. These mutations were created because they render the β2 subunit more like
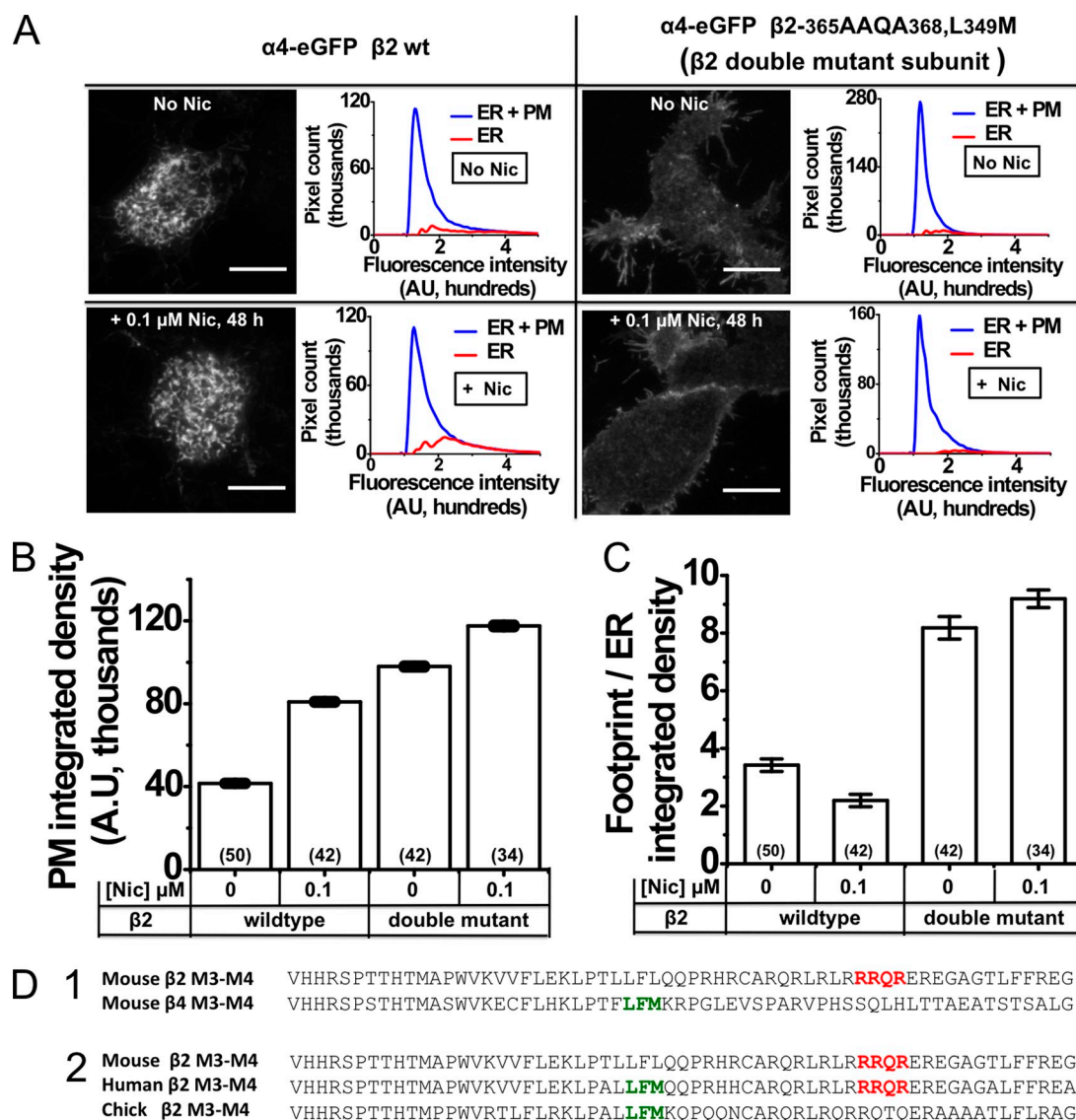
Figure 2. Effect of nicotine, ER export, and retention/retrieval motifs on nAChR expression at the PM. (A) Representative TIRFM images of Neuro-2a cells transfected with α4eGFP β2wt and α4eGFP β2-365AAQA368 L349M double-mutant receptors. Column labels indicate the expressed receptors. Panels indicate the nicotine treatment condition. Bars, 10 µm. Each image is accompanied by a graph plotting the fluorescence intensity (x axis) versus number of pixels (y axis) for whole TIRF footprint (ER + PM) and ER. (B) Bar graph quantifying the PM-integrated density for α4eGFP plus β2wt and α4eGFP plus β2 double-mutant–transfected cells. Transfected β2 subunits and nicotine treatment conditions are indicated below the x axis. Error bars show 99% confidence intervals. (C) Integrated density ratios of whole TIRF footprint to ER for α4eGFP β2wt and α4eGFP β2 double-mutant nAChRs. The transfected β2 subunit and nicotine treatment conditions are indicated below the x axis; error bars are SEM. The number of imaged cells is indicated in parentheses. (D; 1 and 2) Protein sequence alignments of ER export and retention motifs within the M3–M4 loop of β2 and β4 subunits. ER export motifs are in green, and ER retention/retrieval motifs are in red. 1, protein sequence comparison for mouse β2 and β4 subunits; 2, cross-species comparison of the M3–M4 cytoplasmic loop sequences for mouse, human, and chicken β2 nAChR subunits. All β2 sequences include amino acids 321–382, and the β4 sequence includes amino acids 318–378.

the β4 subunit in two regions thought to govern traffic from the ER (Fig. 2 D); thus, the "enhanced ER export" mouse β2 double-mutant subunit (β2-365AAQA368 L349M) contains a disrupted ER retention motif (AAQA) and a reconstituted ER export motif (LFM). The β2 and β4 sequences are strikingly similar in all other regions. Unlike wt α4eGFPβ2 nAChRs, which showed little or no vesicular dynamics (Video 1), α4eGFPβ2-enhanced ER export double-mutant receptors displayed many 0.5–1-μM vesicles trafficking within the TIRFM footprint (Video 3).

In the absence of nicotine, the α4eGFPβ2 double-mutant nAChRs showed a 2.36-fold increase in PM-integrated density compared with wt receptors. 48-h exposure of α4eGFPβ2 double-mutant nAChRs to 0.1 μM nicotine caused only a small additional increase in PM-integrated density (1.2-fold), suggesting that enhanced ER export β2 double-mutant subunits produced nearly maximal anterograde trafficking of nAChRs, even in the absence of nicotine.

To quantify the effects of nicotine and α4eGFPβ2 enhanced ER export double-mutant nAChRs on ER fluorescence (see Materials and methods), we measured the ratio of integrated densities for the whole TIRF footprint to ER-localized signals (footprint/ER ratio; Fig. 2 C). As noted above, the footprint/ER ratio for α4-eGFPβ2wt transfected cells was 3.42, and nicotine treatment reduced the footprint/ER ratio to 2.19, indicating that nicotine also caused an increase in the proportion of nAChRs localized in the ER. The footprint/ER ratio for α4eGFPβ2 double-mutant nAChR-transfected cells was 8.18, a 2.4-fold increase over the ratio observed for α4eGFPβ2wt-transfected cells. Treatment of α4eGFPβ2 double-mutant nAChR-transfected cells with 0.1 μM nicotine for 48 h increased the footprint/ER ratio only slightly further, to 9.19.

Collectively, these results show the following: (a) nicotine causes an up-regulation of wt α4β2 nAChRs at the PM; (b) the β2 subunit possesses an ER export motif (LFM) and an ER retention/retrieval motif (RRQR) that can influence the anterograde trafficking of β2* nAChRs; and (c) nicotine up-regulates enhanced ER export double-mutant nAChRs at the PM to a smaller extent than wt receptors.

Evidently, our experiments depend heavily in quantifying expressed fluorescent proteins (FPs). In gene transfer experiments, quantitative analysis of protein function can be vitiated by several mechanisms that cause a "ceiling," "maximum," "limit," "plateau," "leveling off," or "saturation" of function. Our experiments used transient transfection in the neuron-like Neuro-2a cell expression system. Previous studies using both fluorescent gamma amino butyric acid transporters and fluorescent nAChRs established that, under the conditions used, membrane protein expression levels have not reached maximum (Drenan et al., 2008; Imoukhuede

et al., 2009; Moss et al., 2009; Son et al., 2009). These conditions render the optical assays appropriately sensitive to mutations or pharmacological agents.

Analysis of M3-M4 loop ER retention/retrieval motifs

Because a majority of α4β2 nAChRs localized to the ER, we were interested in analyzing putative ER export and ER retention/retrieval signals and their effects on nicotine-induced up-regulation. We sought to separately quantify the effects of RRQR ER retention/retrieval (Fig. 3) and LFM ER export (Fig. 4) motifs.

We first present data on putative ER retention/retrieval signals, as revealed by the behavior of the β2-365AAQA368 subunit. Mouse β2 subunits possess an RRQR sequence (amino acids 365–368) that is absent in mouse β4 (Fig. 2 D, 1). RRQR motifs are thought to prevent the exit of cargo from the ER and may additionally function as ER retrieval motifs via the binding of the RRXR domain to COPI proteins (Scott et al., 2001, 2003; Brock et al., 2005; Michelsen et al., 2005). A cross-species comparison of mouse, human, and chicken β2 subunit sequences shows that, unlike mouse subunits, human and chicken β2 subunits possess an intact LFM motif, whereas chicken β2 subunits contain an RQTQ sequence in place of the RRQR motif (Fig. 2 D, 2).

Neuro-2a cells were transfected in duplicate as follows: pCS2-mcherry plus α4-eGFP plus β2wt and pCS2-mcherry plus α4-eGFP plus β2-365AAQA368. One set of transfected cells was treated with nicotine (0.1 μM for 48 h), and dual-color TIRF images were obtained. α4-eGFP enabled the localization of nAChRs, and pCS2-mcherry enabled the simultaneous localization of PM.

Fig. 3 A shows representative TIRF images of Neuro-2a cells expressing α4-eGFPβ2-365AAQA368 nAChRs in the absence or presence of nicotine (0.1 μM Nic, 48 h). β2-365AAQA368 subunits increased PM localization of nAChRs, and this effect was enhanced after exposure to nicotine. As described in Materials and methods and previous Results sections, we used pixel-by-pixel measurements of PM-integrated density and a ratio of whole TIRF footprint to ER-integrated density to quantify these effects. Fig. 3 B summarizes the results from PM-integrated density measurements. When compared with wt receptors, α4-eGFPβ2-365AAQA368 nAChRs showed a 1.74-fold increase in the PM intensity, almost equivalent to that observed for nicotine-treated α4-eGFPβ2wt nAChRs. When compared with untreated α4-eGFP β2-365AAQA368–expressing cells, nicotine treatment resulted in a further 1.65-fold increase in the PM-integrated density of α4-eGFPβ2-365AAQA368.

Fig. 3 C (1 and 2) shows graphs plotting the number of ER or ER plus PM pixels against fluorescence intensity. Neuro-2a cells expressing α4-eGFPβ2-365AAQA368 nAChRs showed an increase in the number of PM-localized pixels, an effect that was enhanced after

treatment with 0.1 µM nicotine for 48 h. Fig. 3 D quantifies the integrated density ratios of the whole TIRF footprint to ER in each case. The footprint/ER ratio for α4-eGFPβ2wt–transfected cells was 3.42, whereas nicotine treatment caused a significant reduction in the peripheral ER pixels of α4-eGFPβ2wt receptors (footprint/ER ratio = 2.19). When compared with non-nicotine–treated wt α4-eGFPβ2 nAChRs, the PM fraction of α4-eGFPβ2-365AAQA368 receptors was increased by 2.4-fold (footprint/ER ratio = 5.33), whereas nicotine treatment resulted in a further 1.6-fold increase in PM-localized α4-eGFPβ2-365AAQA368 receptors (footprint/ER ratio = 8.53).

These data show that β2-365AAQA368 subunits markedly increase the localization of receptors in the PM and reduce their localization in the ER, consistent with the presence of an ER retention/retrieval motif in the mouse β2 M3-M4 loop. Mutation of this motif interacts with nicotine treatment to further up-regulate nAChRs at the PM and increases the export of nAChRs from the ER, thus causing a net depletion of ER-localized receptors.

Analysis of ER export motifs

Previous x-ray crystallographic and biochemical studies show that I/LXM (where X is any amino acid)-packaging motifs in ER cargo such as membrin and syntaxin 5 bind to a surface groove of Sec24D, which is a major component of COPII vesicles (Mancias and Goldberg, 2008). In a perhaps oversimplified view, this binding partially enables the packaging of ER cargo into COPII vesicles at ERES. Sequence alignments showed that the mouse β4 M3–M4 large intracellular loop contains an LFM motif (amino acids 344–346), whereas mouse β2 subunits possess a leucine residue at position 349, resulting in an LFL sequence at the aligning positions (Fig. 2 D, 1).

To elucidate the role of LFM motifs on the ER export of nAChRs, we mutated the LFM motif in the α4-eGFP subunit to AFM (called α4L358A-eGFP) and the LFL motif in β2wt subunits to LFM (called β2-L349M). We reasoned that these point mutations enabled the expression of specific receptor combinations containing (a) zero LFM motifs (α4L358A-eGFP plus β2wt), (b) two to three LFM motifs (α4-eGFP plus β2wt), or (c) five
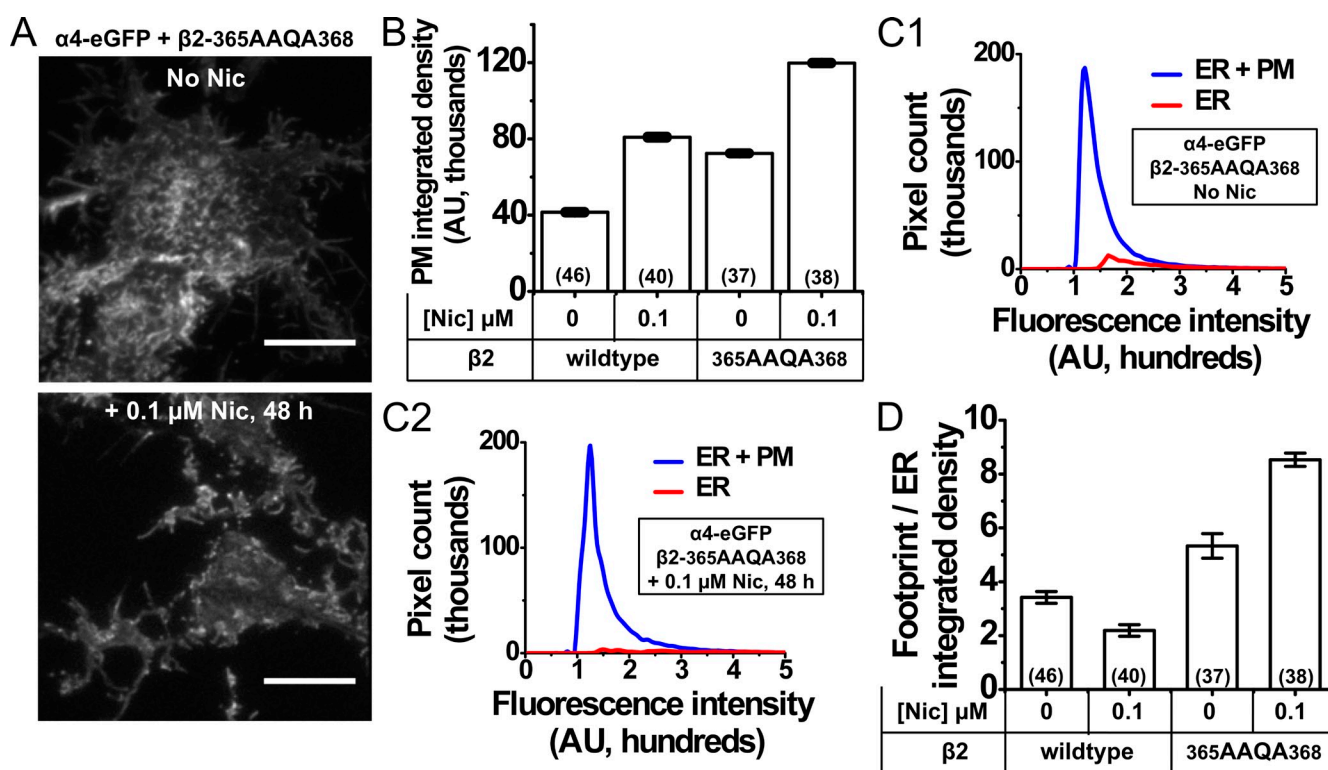

Figure 3. Effect of the β2 M3–M4 loop ER retention/retrieval motif on PM trafficking of α4β2 nAChRs. (A) Representative TIRFM images of α4eGFP plus β2-365AAQA368–transfected cells. Nicotine treatment conditions are indicated for each image; bars, 10 µM. (B) Integrated density for α4eGFP plus β2wt– and α4eGFP plus β2-365AAQA368–transfected cells. Transfected β2 subunits and nicotine treatment conditions are indicated below the x axis; the numbers of imaged cells are indicated within the parentheses; error bars show 99% confidence intervals. (C, 1 and 2) Line graphs plotting the pixel number versus fluorescence intensity for whole TIRF footprint (ER + PM) or the ER for α4eGFP plus β2-365AAQA368–transfected cells with and without nicotine as indicated. (D) Integrated density ratios of whole TIRF footprint to ER for α4eGFP β2wt and α4eGFP β2-365AAQA368 nAChRs; error bars are SEM. The transfected β2 subunit and nicotine treatment conditions are indicated below the x axis. The numbers of imaged cells are indicated in parentheses.

LFM motifs (α4-eGFP plus β2-L349M). This allowed us to correlate the PM expression of receptors with the number of LFM motifs present in receptor pentamers.

To assess the effect of LFM motifs on ER export and PM localization of mutant receptors, Neuro-2a cells were transfected with pCS2-mcherry (PM marker) and α4-eGFP plus β2wt (two to three LFM motifs), α4-eGFP plus β2-L349M (five LFM motifs), or α4L358A-eGFP plus β2wt (zero LFM motifs). In all cases, eGFP fluorescence was used to report the localization of nAChRs. Fig. 4 A shows representative images of TIRF footprints from each transfection. ~90% of α4-eGFP plus β2wt–transfected cells showed ER- and PM-localized receptors (Fig. 4 A, first column). 50% of α4-eGFPβ2-L349M–transfected cells showed a mixed ER plus PM localization, and the remaining 50% showed TG/TGN- and PM-localized nAChRs (Fig. 4 A, second and third columns). In contrast, receptors in ~90% of α4L358A-eGFPβ2wt–transfected cells primarily localized to the ER (Fig. 4 A, fourth column), and the remaining 10% of cells did not yield clear TIRF footprints. Fig. 4 B quantifies the observed differences in the PM-integrated
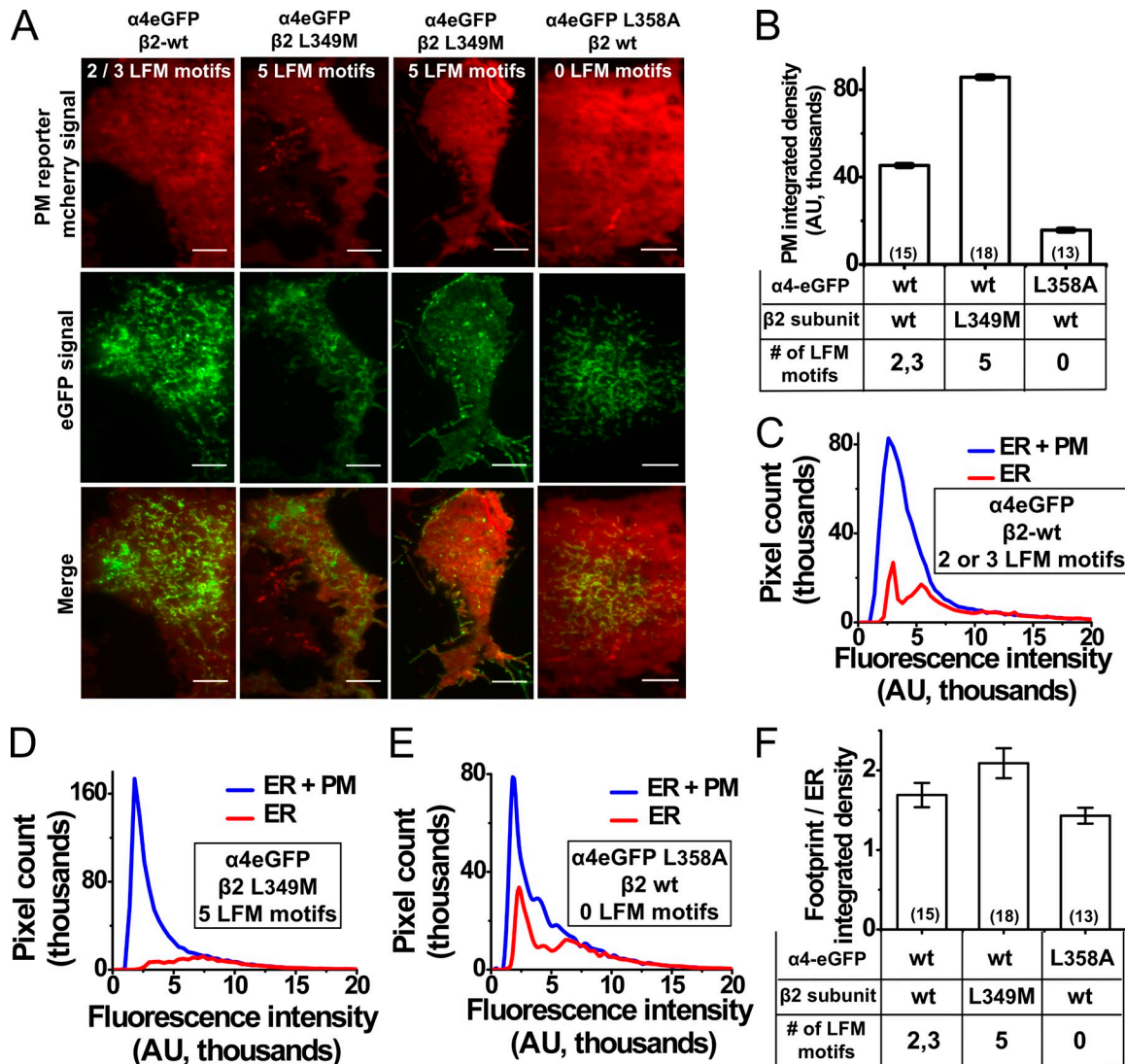

Figure 4. Effect of β2 M3–M4 loop ER export motifs on PM trafficking of α4β2 nAChRs. (A) Representative TIRF images of mouse Neuro-2a cells transfected with a PM mcherry reporter and either α4eGFP plus β2wt (assembled receptors possess two to three LFM motifs), α4eGFP plus β2L349M (five LFM motifs), or α4eGFPL358A plus β2wt (zero LFM motifs). Bars, 5 µm. (B) PM-integrated densities for α4eGFP plus β2wt–, α4eGFP plus β2-L349M–, and α4eGFPL358A plus β2wt–transfected cells. Transfected subunits and the number of LFM motifs per pentamer are indicated below the x axis; error bars show 99% confidence intervals. The number of imaged cells is indicated in parentheses. (C–E) Pixel number versus fluorescence intensity for whole TIRF footprint (ER + PM) or the ER in α4eGFP plus β2wt–, α4eGFP plus β2L349M–, and α4L358AeGFP plus β2wt–transfected cells. (F) Integrated density ratios of whole TIRF footprint to ER for α4eGFP plus β2wt–, α4eGFP plus β2L349M–, and α4L358AeGFP plus β2wt–transfected cells; error bars are SEM. Transfected subunits and the number of LFM motifs per pentamer are indicated below the x axis. The numbers of imaged cells are indicated in parentheses.

density for wt and mutant nAChRs. The α4-eGFPβ2-L349M nAChRs showed a 1.9-fold increase in the PM-integrated density over α4-eGFPβ2wt nAChRs, whereas α4L358A-eGFPβ2wt nAChRs showed a 2.9-fold reduction in PM-integrated density when compared with α4-eGFPβ2wt nAChRs.

Whole TIRF footprint to ER-integrated density ratios were used to quantify the observed differences in the subcellular localization of wt and mutant nAChRs. The number of pixels representing either the ER or ER plus PM was plotted against fluorescence intensity (Fig. 4, C–E), and a ratio of the whole TIRF footprint to ER-integrated density (footprint/ER ratio) was used to compare the extent to which receptors localized to the ER or post-TG/TGN and PM compartments (Fig. 4 F). Results showed a 1.25-fold increase in the ratio of α4-eGFPβ2-L349M (footprint/ER ratio = 2.09) as compared with α4-eGFPβ2wt nAChRs (footprint/ER ratio = 1.69), whereas α4L358A-eGFPβ2wt–transfected cells showed a small reduction in the integrated density ratio (footprint/ER ratio = 1.43). Collectively, these results demonstrate that LFM motifs in the M3–M4 loop of α4 and β2 subunits alter the ratio of receptors localized within the cellular PM versus the ER, and that the PM nAChR number increases monotonically with the number of LFM export motifs present in receptor pentamers.
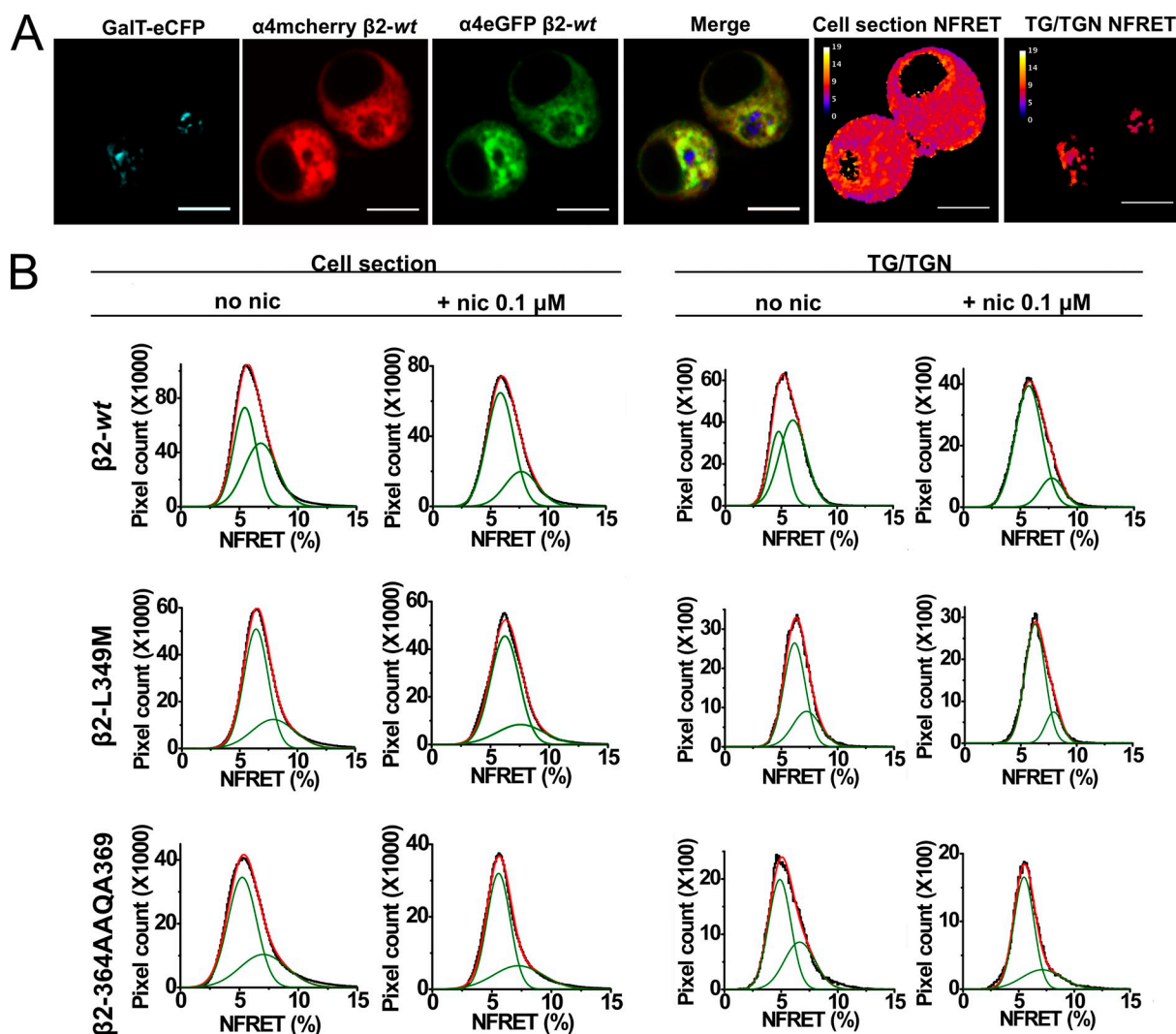
Figure 5. NFRET measurements of the effects of nicotine and β2 M3–M4 loop mutations on α4β2 nAChR stoichiometry. (A) Representative confocal images of Neuro-2a cells expressing a TG/TGN marker (GalT-eCFP) and α4-eGFP plus α4-mcherry plus β2wt nAChRs. FP tags (FP = any FP) were used to obtain the trans-Golgi ROI and to separately measure pixel-based NFRET values for either the whole cell section or for the TG/TGN. Bars, 5 µm. (B) Frequency plots of NFRET values (x axis) versus number of pixels (y axis) for α4-eGFP plus α4-mcherry coexpressed with β2wt/β2-L349M/β2-365AAQA368 subunits. Pixel-based NFRET values were separately obtained in the presence or absence of 0.1 µM nicotine (nic) as indicated. Column labels show the ROI for NFRET measurements (whole cell section or TG/TGN), and row labels show the type of β2 subunit (β2wt/β2-L349M/β2-365AAQA368) coexpressed with α4-eGFP plus α4-mcherry. Frequency histograms (black) were fitted to two Gaussian components (green) with low $(\alpha4)_2(\beta2)_3$ and high $(\alpha4)_3(\beta2)_2$ mean NFRET values. Overall fits (red) are shown for each graph; data are quantified in Table I.

Alternative analyses of the TIRFM data

We consider that pixel-based TIRF fluorescence intensity analyses of Figs. 1–4 represent the most appropriate analysis of the measurements. To test the robustness of the TIRF data, we conducted two alternative analyses. First, we calculated the data of Figs. 1–4 on a cell-by-cell basis: pixel sums and averages for the ER and PM of each cell. For these cell-by-cell data, which thus concerned 15–50 cells per condition, we defined statistical significance as P < 0.01. Differences calculated with this method were also significant when the pixel-based analyses showed significance.

Second, we calculated the pixel-based data by simply counting the number of pixels in the ER and PM categories, rather than by taking the average and summed intensities. Again, we found patterns similar to those of Figs. 1–4. Thus, the data of Figs. 1–4 satisfy two additional tests.

Effect of nicotine and β2 M3–M4 loop motifs on the stoichiometry of assembled α4β2 receptors: NFRET analysis

Our TIRFM experiments show that incubation in nicotine, or manipulation of ER export and ER retention/ retrieval motifs in the M3–M4 loop of nAChRs, increases nAChR PM expression. Because nicotine is thought to increase the assembly of receptors with a $(\alpha4)_2(\beta2)_3$ stoichiometry (Nelson et al., 2003; Son et al., 2009), and because $(\alpha4)_2(\beta2)_3$ receptors contain only two LFM ER export motifs, we reasoned that the effects of nicotine on increased ER-localized receptors may partially occur as a result of the increased assembly of $(\alpha4)_2(\beta2)_3$ receptors. We therefore used FRET analysis to characterize the effect of nicotine and β2 subunit mutations on nAChR stoichiometry. Pixel-based NFRET is an appropriate method to determine the stoichiometry of protein complexes in Neuro-2a cells (Moss et al., 2009; Son et al., 2009). Our previous work exploited the idea that in cells expressing equal numbers of α4 subunits tagged with donor or acceptor FPs (α4-FP subunits plus untagged β2 subunits), 50% of nAChRs with the $(\alpha4)_3(\beta2)_2$ stoichiometry possess adjacent donor and acceptor α4-FP subunits. These nAChRs show greater NFRET values than the $(\alpha4)_2(\beta2)_3$ nAChR stoichiometry, which has nonadjacent donors and acceptors (Son et al., 2009). Our previous work used confocal microscopy to show that the ER forms the primary intracellular compartment of Neuro-2a cells (Moss et al., 2009). In whole cell optical sections, the majority of the intracellular fluorescent signal from α4-FPβ2 nAChRs also localizes to the ER. This agrees with previous observations (Hill et al., 1993; Commons, 2008). Our NFRET experiments used a GalTeCFP marker to delineate the trans-Golgi apparatus, where we find most of the remaining intracellular α4-FPβ2 nAChRs. It has not been possible to systematically study NFRET in the additional structures present in our optical sections: unlabeled COPI/COPII structures, peripheral trafficking vesicles, endosomes, and lysosomes.

We measured NFRET pixel distributions to assess the effect of nicotine exposure (0.1 µM for 48 h) on nAChR stoichiometry, either for the whole cell section or within the TG/TGN. Frequency histograms of NFRET values (x axis) versus number of pixels (y axis) were fitted to Gaussian components (Fig. 5 B). A coefficient of determination (R^2) value of 0.995 served as a criterion to determine the number of components required for the fit. Our analysis, summarized in Table I, used the parameters A1 and A2 that correspond to the total pixels contributing to lower and higher NFRET components, which represent the $(\alpha4)_2(\beta2)_3$ and $(\alpha4)_3(\beta2)_2$ nAChR stoichiometries, respectively. We assign more importance to the fractional area (number of pixels) for each component, for instance A1/(A1 + A2), than to the shifts in positions of the mean NFRET values, because the NFRET algorithm provides only an approximate normalization for pixel intensity. In the case of whole cell section NFRET measurements, 48-h nicotine exposure caused an increase in the proportion of $(\alpha4)_2(\beta2wt)_3$ nAChR pixels, from A1/(A1 + A2) = 0.51 to 73, in the whole cell section ROI.

We directly tested for pharmacological chaperoning in the ER by assessing whether the subunit alterations reached completion by the time the nAChRs reached the TG/TGN. Neuro-2a cells were cotransfected with four plasmids: a GalT-eCFP TG/TGN marker plus α4-eGFP (FRET donor) plus α4-mcherry (FRET acceptor) plus β2 subunit. The use of GalT-eCFP thus enabled us to isolate NFRET measurements of receptors within the TG/TGN (Fig. 5 A). NFRET in wt and mutant receptors was measured for either the whole cell section or the TG/TGN ROI in the absence or presence of nicotine (0.1 µM for 48 h; Fig. 5 A).

We also compared the stoichiometry data for mutant and wt β2 subunits. As noted above, α4β2wt assembled as $(\alpha4)_2(\beta2wt)_3$ and $(\alpha4)_3(\beta2wt)_2$ receptors, with a

TABLE I
Change in α4β2 stoichiometry in the presence of nicotine (0.1 µM for 48 h)

β2 subunit	Whole cell section			TG / TGN		
wt	0.51	vs.	0.73	0.36	vs.	0.83
L349M	0.70	vs.	0.79	0.69	vs.	0.82
365AAQA368	0.67	vs.	0.70	0.63	vs.	0.74

Note that effects of nicotine and of β-subunit ER export mutations appear to approach a common value of increased $(\alpha4)_2(\beta2)_3$ stoichiometry. NFRET measurements were fitted to Gaussian components, as in Fig. 5, yielding the total pixel area under either the A1 (lower NFRET) or A2 (higher NFRET) components. These components correspond, respectively, to $(\alpha4)_2(\beta2)_3$ and $(\alpha4)_3(\beta2)_2$ stoichiometry. Each number is the ratio of areas, A1/(A1 + A2). The entries denote control solution versus nicotine exposure in either the whole cell section or the Golgi apparatus (TG/TGN).

nearly equal proportion of pixels containing the two stoichiometries: $A1/(A1 + A2) = 0.51$. However $A1/(A1 + A2)$ for $\alpha4\beta2$-L349M and $\alpha4\beta2$-365AAQA368 receptors were greater (0.70 and 0.63, respectively), indicating an increased proportion of nAChRs possessing a $(\alpha4)_2(\beta2$-L349M$)_3$ and $(\alpha4)_2(\beta2$-365AAQA368$)_3$ stoichiometry. As noted above, in the TG/TGN, we observed $A1/(A1 + A2) = 0.36$ for $\alpha4\beta2$wt; on the other hand, $\alpha4\beta2$-L349M and $\alpha4\beta2$-365AAQA368 nAChRs yielded 0.69 and 0.73, respectively.

NFRET measurements on the TG/TGN ROI showed that nicotine induced a dramatic increase in the proportion of $(\alpha4)_2(\beta2$wt$)_3$ nAChR pixels, from $A1/(A1 + A2) = 0.36$ to 0.83. For the $(\alpha4)_2(\beta2$-L349M$)_3$ nAChR, nicotine induced a change in $A1/(A1 + A2)$ from the already elevated value of 0.69 to 0.82. The already elevated nicotine-free value of 0.63 for $(\alpha4)_2(\beta2$-365AAQA368$)_3$ pixels was further increased by nicotine to 0.74.

Nicotine exposure also produced only a minor increase in the already elevated whole cell section ROI $A1/(A1 + A2)$ values for the $\beta2$ subunits with enhanced export mutations. For $(\alpha4)_2(\beta2$-L349M$)_3$ nAChR pixels, nicotine increased $A1/(A1 + A2)$ from 0.70 to 0.79. The analogous effect for the $(\alpha4)_2(\beta2$-365AAQA368$)_3$ nAChR pixels was a change from 0.67 to 0.70.

Collectively, NFRET analyses show that wt and mutant $\alpha4\beta2$ nAChRs assemble with both $(\alpha4)_2(\beta2)_3$ and $(\alpha4)_3(\beta2)_2$ stoichiometries in the ER. Both nAChR stoichiometries traffic to the TG/TGN, but nAChRs with the mutant $\beta2$ subunits studied here demonstrate a relatively high proportion of $(\alpha4)_2(\beta2)_3$ nAChRs. In all cases, 48-h nicotine exposure increased the proportion of nAChRs with a $(\alpha4)_2(\beta2)_3$ stoichiometry. This increase was most marked with wt nAChRs, which show the weakest bias toward the $(\alpha4)_2(\beta2)_3$ stoichiometry in the absence of nicotine, as though (a) treatment with nicotine and mutations enhancing ER exit have similar effects of enhancing $(\alpha4)_2(\beta2)_3$ stoichiometry; and (b) these effects partially occlude each other, reaching a common maximal value in which 0.75–0.8 of the nAChRs possess the $(\alpha4)_2(\beta2)_3$ stoichiometry.

Nicotine and β2 M3–M4 loop motif mutants increase ERES numbers

Our data show that both incubation in nicotine and specific trafficking motifs within the $\beta2$ M3–M4 loop can influence the subcellular localization and trafficking of assembled nAChRs. We therefore sought to understand the effect of $\beta2$ M3–M4 loop motifs on nAChR trafficking at a stage that is distal in the ER but still relatively early in the secretory pathway. Because a component of the COPII ERES complex, Sec24D, binds to IXM motifs of vesicular proteins syntaxin 5 and membrin (Mancias and Goldberg, 2008), one expects the formation of ERES to increase with the number of Sec24D molecules recruited by LFM motifs within assembled nAChRs.

Our initial experiments addressed the hypothesis that some $\alpha4\beta2$ nAChRs localize near ERES. We used TIRFM, which can localize fluorophores with high resolution in the z axis as well as the x–y plane. Like nearly all cells studied, Neuro-2a cells presumably have a complement of endogenous Sec24 isoforms; we expressed additional FP-labeled Sec24D. TIRF videos of Neuro-2a cells cotransfected with $\alpha4$-mcherry plus $\beta2$wt plus Sec24D-eGFP showed that coexpression of Sec24D, even with wt nAChRs and in the absence of nicotine, produced additional dynamic features in the nAChR population, as though the addition of Sec24D increases the proportion of nAChRs exiting the ER. nAChRs do appear near ERES; furthermore, nAChRs seem to move near and, in some cases, through ERES or past ERES (Video 4). In the presence of nicotine (0.1 µM for 48 h), the ERES were at least as plentiful (Video 5).

We therefore conducted two series of quantitative studies on ERES number. First, we studied the effect of nicotine exposure on ERES numbers. Because results presented above agree with the hypotheses that nicotine exposure increases the number of nAChRs that exit the ER and reach the PM, we asked whether this increased flux recruited additional ERES to participate in ER exit. Neuro-2a cells were transfected with Sec24D-mcherry, either alone or with $\alpha4$-eGFP plus $\beta2$-wt, or with the *Caenorhabditis elegans* GluCl α plus β subunits (Fig. 6 E) (Slimko et al., 2002). Cells were exposed either to control solution or to nicotine (0.1 µM for 48 h). In Fig. 6 E, the first set of bars show that nicotine had no effects on ERES number in the absence of nAChR expression. However, when ERES were counted in cells transfected with $\alpha4\beta2$ nAChRs, nicotine caused a twofold increase in ERES from ∼25 to ∼50 per cell (Fig. 6 E). This effect of nicotine was specific to nAChR expression because nicotine did not increase ERES in parallel control experiments of cells transfected with *C. elegans* GluCl.

Second, to test the effect of increasing LFM motifs per nAChR pentamer on ERES formation, Neuro-2a cells were separately transfected with wt and mutant nAChR combinations as follows: $\alpha4$L358A-eGFP plus $\beta2$wt (zero LFM motifs), $\alpha4$-eGFP plus $\beta2$wt (± nicotine; two or three LFM motifs), $\alpha4$L358A-eGFP plus $\beta4$wt (two or three LFM motifs), $\alpha4$-eGFP plus $\beta2$-L349M (five LFM motifs), and $\alpha4$-eGFP plus $\beta4$wt (five LFM motifs). In each case, cotransfected Sec24D-mcherry served as a reporter for quantifying ERES number. Fig. 6 A shows representative confocal images of a Neuro-2a cell cotransfected with $\alpha4$-eGFP plus $\beta2$wt plus Sec24D-mcherry. Sec24D-mcherry–positive ERES particles were demarcated using intensity-based thresholding and were counted for each cell.

Fig. 6 B summarizes the results obtained from three independent experiments. ∼17 ERES per cell were observed with $\alpha4$L358A-eGFP$\beta2$wt receptors, whereas $\alpha4$-eGFP$\beta2$wt receptors showed ∼30 ERES per cell.

α4-eGFPβ2-L349M receptors showed ∼52 ERES per cell, which was significantly different from α4-eGFPβ2wt receptors (two-tailed *t* test; P < 0.001). α4-eGFPβ4wt receptors demonstrated ∼47 ERES per cell, which was significantly higher than the number of ERES (∼34 per cell) in α4L358A-eGFPβ4wt–transfected cells (P < 0.01). When ERES number (y axis) is displayed versus the number of LFM motifs (x axis) per pentamer, the average number of ERES increased monotonically with the number of LFM export motifs present in wt and mutant nAChRs (Fig. 6 C). In parallel experiments, quantification of ERES number in α4-eGFPβ2-365AAQA368–transfected cells showed an average of ∼38 ERES per cell, which was significantly higher than α4-eGFPβ2wt–transfected cells (∼20 ERES per cell; P < 0.01; Fig. 6 D). Collectively, these data show that mutations in the M3–M4

loop of α4 and β2 subunits can influence ERES numbers and the rate of ER exit of nAChRs, either by affecting Sec24D binding to LFM motifs or by preventing the ER retention of nAChRs through an RRQR motif in the mouse β2 M3–M4 loop.

Simulating effects of nicotine and β2 subunit mutations on nAChR assembly and trafficking

In a quantitative model for the experiments, we focused on six target measures. We sought to explain the enhancement of PM fluorescence by nicotine treatment (Fig. 2 B, first two columns; target measure 1). Four of the measures include the data of Fig. 2 C. For the wt nAChR, nicotine produces a substantial decrement in the integrated density ratio of whole TIRF footprint to ER-localized receptors (from 3.42 to 2.19; target
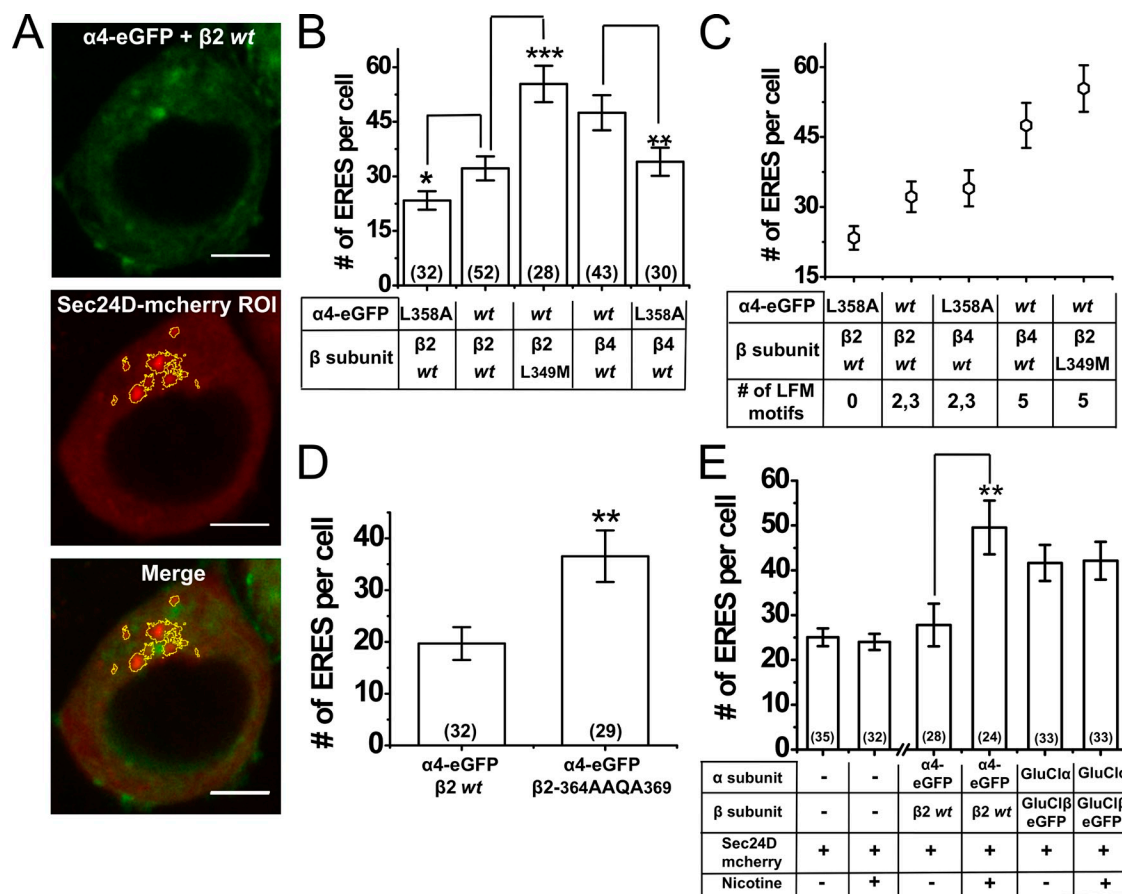
Figure 6. Effect of α4 and β2 ER export motifs, β2 ER retention/retrieval motifs, and nicotine exposure on ERES. (A) Representative confocal images of a Neuro-2a cell transfected with α4-eGFPβ2wt nAChRs and an ERES marker, Sec24D-mcherry. ROI representing Sec24D-mcherry ERES structures are demarcated, and a merged image of α4-eGFPβ2wt plus Sec24D-mcherry is shown. Bars, 5 µm. (B) Average number of ERES per cell for α4-eGFPL358Aβ2–, α4-eGFPβ2wt–, α4-eGFPβ2L349M–, α4-eGFPβ4wt–, and α4-eGFPL358Aβ4wt–transfected cells. (C) Scatter plot of number of ERES per cell for α4-eGFPL358Aβ2–, α4-eGFPβ2wt–, α4-eGFPL358Aβ4wt–, α4-eGFPβ4wt–, and α4-eGFPβ2L349M–transfected cells. (D) Number of ERES per cell for α4-eGFPβ2wt– and α4-eGFPβ2-365AAQA368–transfected cells. (E) Number of ERES per cell in untreated and nicotine-treated (0.1 µM for 48 h) cells transfected either with no additional proteins, with α4-eGFPβ2wt nAChRs, or with GluClαwtGluClβ-eGFP. The number of cells imaged is indicated in parentheses; data are mean values ± SEM. NS, not significant; *, P = 0.06; **, P < 0.01; ***, P < 0.001, two-tailed *t* test. The break on the horizontal axis indicates sets of experiments that were performed on different batches of cells; therefore, the absolute numbers of ERES may not be directly comparable between batches.

measures 2 and 3, respectively). However, for the enhanced ER export β2 mutant nAChR, the ratio is larger (8.18) but is only slightly increased by nicotine (9.19; target measures 4 and 5, respectively). We suspected that nAChRs encounter a step(s) in exiting the ER that acts as a bottleneck for wt nAChRs, but not for the enhanced ER export mutant. Target measures 1–5 are based on TIRFM data.

Finally, we also sought to simulate a measurement based on confocal microscopy: the enhancement of ERES by nicotine (1.78-fold; Fig. 6 E; target measure 6).

We developed a formal kinetic model that explains these phenomena, that provides kinetic terms consistent with the suspected functional changes in the enhanced ER export mutations, and that incorporates the chaperoning function of nicotine in the ER. The

scheme is based on FOLDEX (Wiseman et al., 2007), on a model for ERES formation (Heinzer et al., 2008), and also on SePhaChARNS (Lester et al., 2009).

The mutation-sensitive step in ER exit has a limited flux capacity in units of molecules/second; if expressed as a rate constant in units of s^{-1}, the rate constant decreases with increasing numbers of nAChR molecules. This concept could be formalized in several ways. We chose to retain the FOLDEX description in which step 9 combines cargo (nAChRs in this case) and molecules from an unspecified pool of export machinery. Importantly for our formulation, this pool can be depleted. The resulting complex condenses to form ERES (several dozen export machinery–nAChR complexes presumably form each ERES or transport vesicle) (Russell and Stagg, 2010). Step 9 has reversible Michaelis-Menten kinetics.
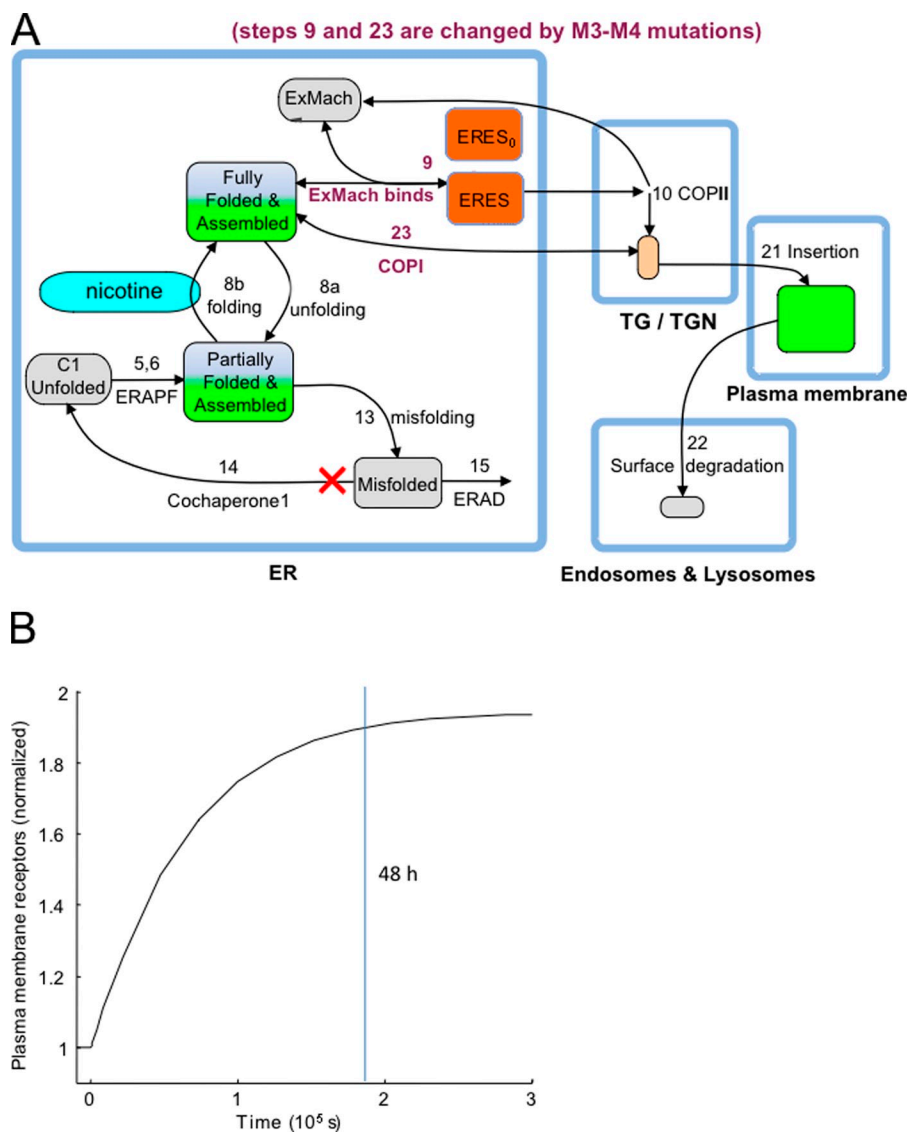
Figure 7. Simulation of nicotine-induced nAChR up-regulation. The experimental data are explained by a pharmacological chaperoning and trafficking scheme based on FOLDEX (Wiseman et al., 2007) and on a model for ERES formation (Heinzer et al., 2008). (A) The SePhaChARNS 2.0 model for explaining target measures 1–6. The reactions numbered <20 are identical to those of Wiseman et al. (2007); FOLDEX has been simplified for the SePhaChARNS 2.0 model. The reaction steps in purple type are influenced by the M3–M4 trafficking mutations. The nAChRs in partially and fully folded ER compartments are shown with gradient fills to denote that only near-membrane molecules are visible in TIRFM. FOLDEX step 14 (involving a protein co-chaperone) is inactivated in the present model because we have little information about protein co-chaperones in the present context. Reactions numbered >20 are added for the SePhaChARNS 2.0 model, which includes post-ER events. The ERES$_0$ population comprises ERES that are visible with Sec24D-mcherry but associated with other cargo molecules or that reside in ER regions not containing nAChRs. ExMach, unspecified export machinery; ERAPF, ER-associated partial folding; ERAD, ER-associated degradation. (B) The simulated course of up-regulation at the PM for the exemplar parameters. The simulation was allowed to reach steady state (at nicotine = 0.0033 µM) before the period indicated. At time zero, the nicotine concentration was jumped to 0.1 µM. A vertical line is shown at 48 h = 1.9 × 10^5 s, the time of the measurements; parameters were chosen based on this time point.

TABLE II

Exemplar parameters that provide good fits to the six target measures

Step	Rate constant name	Exemplar value	
		wt	Enhanced ER export mutant
Reactions			
5,6	k_C1→U	0.011 s^{-1}	
8a	k_U→F	$33 \times 10^6 \text{ M}^{-1}\text{s}^{-1}$	
8b	k_F→U	0.012 s^{-1}	
9	k_F→ERES	$499 \text{ M}^{-1}\text{s}^{-1}$	$734 \text{ M}^{-1}\text{s}^{-1}$
	k_ERES→F	0.01 s^{-1}	
10	k_ERES→G	0.034 s^{-1}	
13	k_U→M	0.012 s^{-1}	
14	k_M→C1U	inactive	
15	k_misfolded→ERAD	0.1 s^{-1}	
21	k_Golgi→PM	10^{-4} s^{-1}	
22	k_S→L	$3 \times 10^{-3} \text{ s}^{-1}$	
23	k_Golgi→Folded	0.22 s^{-1}	0.10 s^{-1}
	k_Folded→Golgi	0	

See model Fig. 7 A.

The forward binding rate constant of step 9, k_F→ERES, is one of the two rate constants that we allowed to differ between wt and "enhanced ER exit" mutant nAChRs (the other is k_Golgi→Folded, which governs step 23; see Tables II and III). The COPII ER export machinery molecules are then released at step 10, which is associated with COPI vesicles. There is evidence that COPI can mediate both anterograde and retrograde transport between ER (Stephens et al., 2000), but to keep the model simple, we have set the anterograde rate, k_Folded→Golgi, equal to zero.

We formalized the effect of nicotine as a binding step that helps nAChRs fold and assemble fully (step 8). Because nicotine binds at the subunit interface and therefore aids assembly, we depict nicotine as favoring the forward-folding step, rather than as inhibiting the unfolding (at the level of formal simulations, these differences have no importance; see also Discussion). If further saturable steps (similar to step 9) do not occur, step 8 would govern the dose–response relation for up-regulation. We therefore chose to maintain the K_m of step 8 at a level near the nicotine concentration in our experiments and in previous reports. This is approximately the nicotine concentration that gives half-maximal up-regulation (Kuryatov et al., 2005, 2008). We maintained this K_m (which equals (k_F→U)/(k_U→F) at a value of $\leq 0.2 \text{ }\mu M$ by specifying that k_U→F $\geq 0.05 \times 10^6 \text{ M}^{-1}\text{s}^{-1}$. Note that nAChRs do form in the absence of nicotine; we formalized this concept by defining an endogenous nicotine-like agent with an "effective endogenous concentration of nicotine" that is *n*-fold lower than the 0.1 μM nicotine studied in our experiments.

All other steps in SePhaChARNS 2.0 (Fig. 7 A) follow first-order unidirectional kinetics, governed by rate constants with the dimensions of s^{-1}, as in the FOLDEX model (Wiseman et al., 2007). The model also incorporates a rudimentary acknowledgment that chaperoning changes the subunit stoichiometry of nAChRs. A complete shift, from 100% $(\alpha4)_3(\beta2)_2$ to 100% $(\alpha4)_2(\beta2)_3$, would imply that each chaperoned receptor has two thirds the $\alpha4$ subunit fluorescence of a native receptor. In fact, our experiments and previous data (Buisson and Bertrand, 2001; Nelson et al., 2003; Kuryatov et al., 2005; Sallette et al., 2005; Vallejo et al., 2005; Son et al., 2009) suggest a shift from approximately equal contributions of the two stoichiometries in nicotine-naive cells to

TABLE III

Exemplar parameters that provide good fits to the six target measures

Molecule	Model name	Concentrations
Fixed Concentrations		
Nascent nAChRs	C1 unfolded	10^{-5} M
Endogenous ERES	ERES$_0$	$8 \times 10^{-4} \text{ M}$
Export Machinery	ExMach00	$9.0 \times 10^{-3} \text{ M}$
"Endogenous" nicotine	Nicotine0	3.3 nM
Optical parameter		
Fraction of ER fluorescence detected by TIRF	ER_fractional_signal	0.14

See model Fig. 7 A.

~100% $(\alpha4)_2(\beta2)_3$ after chronic nicotine exposure. SePhaChARNS 2.0 incorporates this change in stoichiometry: we calculate the predicted fluorescence of wt PM up-regulated nAChRs as 0.83 times that of receptors in the absence of nicotine.

Tables II and III give the exemplar parameters that provide a good fit to the six target measures. We consider these parameters physically plausible and expect that they fall within threefold of actual values. The simulations force all molecular concentrations to scale with that of C1 unfolded, the initial constant source of unassembled, unfolded subunits. We arbitrarily chose this measure as 10 µM. The time scale of the calculations is determined primarily by the rates of insertion and removal from the surface PM, k_Golgi→PM and k_S→L. We set k_S→L = 3×10^{-3}/s, somewhat faster than previous reports for wt receptors (Kuryatov et al., 2005). We think it possible that these measurements of Kuryatov et al. (2005) were influenced by events that occur earlier in the pathway, such as k_Golgi→PM. In our formulation, this is the slowest step (k_Golgi→PM = 10^{-4} s^{-1}) and governs the simulated time course of PM up-regulation (shown in Fig. 7 B).

The TIRF evanescent signal penetrates only partially into the cell. Consider that the cell is symmetric about a horizontal plane and that we are simulating the half closest to the coverslip. TIRFM fully visualizes the PM but only a fraction of the internal membranes such as ER. We assign this fraction to the parameter "ER_Fractional_signal." The exemplar parameters are associated with ER_Fractional_signal = 0.14, which seems reasonable based on our further unpublished experiments using higher resolution TIRFM. However, simulations with other acceptable parameter sets were satisfied by values between 0.05 and 0.5.

The simulations revealed that a broad range of parameters simulated target measures 1 through 6 described above. In particular, the simulations verified that ERES formation (step 9) proceeds greater than twofold more efficiently, and COPI-mediated retrieval (step 23) proceeds greater than twofold less rapidly, for $\alpha4\beta2$ nAChRs containing the enhanced ER export mutant $\beta2$ subunit than for nAChRs containing wt $\beta2$ subunits (Tables II and III).

We further constrained the simulations to occur with a minimal effect of nicotine, defined as minimizing n. Satisfactory simulations were achieved if the "effective endogenous nicotine concentration" was ≤0.0033 µM ($n \geq 30$), implying that nicotine incubation improves pharmacological chaperoning by ≥30-fold. With $n = 10$ (an endogenous "effective nicotine concentration" 10-fold lower that the experimental value of 0.1 µM), the simulations were marginally acceptable (sum of squared residuals = 0.0127, with all predicted values in error by <7% difference).

Although the simulation provides adequate explanations for the six target parameters, we also asked whether the optimized parameters predict an additional measurement: the 1.86-fold increased ERES sites in the enhanced ER export $\beta2$ double mutant in the absence of nicotine (Fig. 6, B–D). Here, the model was unsuccessful, simulating the observed increase in ERES numbers only if k_F→ERES for the wt nAChR was ~10-fold lower than the exemplar parameter value. The Discussion notes that additional mechanisms may be required to explain this datum.

The SePhaChARNS 2.0 model therefore provides a reasonable explanation for most of the differential effects of nicotine incubation and of the enhanced ER export $\beta2$ subunit. The model is consistent with the idea that nicotine provides a pharmacological chaperoning effect within the ER, upstream from a flux-limited ER export process, and that this ER export limitation is ameliorated by the (perhaps tautologically named) enhanced ER export $\beta2$ subunit mutant. The chaperoning effect of nicotine appears to enhance an endogenous process by a factor (n) between 10 and 30. The model requires no flux-limited steps that occur after ER export.

DISCUSSION

Up-regulation of nAChRs by chronic nicotine is thought to play major roles both in nicotine dependence and in the inverse correlation between a person's history of tobacco use and his or her susceptibility to Parkinson's disease (see Introduction). This paper addresses up-regulation by chronic nicotine in a cellular system that is especially favorable for optical studies, but because up-regulation is generally observed in clonal cells, neuronal cultures, isolated bronchial epithelium, and intact mice, we have confidence in the study's pathophysiological significance. We studied nAChRs in several compartments before and during up-regulation. To aid in this study, we designed and exploited an enhanced ER export $\beta2$ subunit mutated in the M3–M4 loop with export properties resembling those of $\beta4$ subunits.

We primarily used subcellularly resolved fluorescence microscopy and pixel-by-pixel analysis methods on FP-labeled $\alpha4$ subunits. We cannot state that the FP-labeled subunits perfectly emulate the unlabeled subunit, but our previous measurements have detected no differences between the FP-labeled and unlabeled wt $\alpha4$ subunits. These studies on the FP-$\alpha4$ subunits included electrophysiology, Ca^{2+} flux, ligand binding, cellular and subcellular localization, and mouse behavior. Previous experiments on the $\alpha4$-FP subunits studied both baseline characteristics and up-regulation in transfected neurons (Nashmi et al., 2003), transfected Neuro-2a cells (Drenan et al., 2008; Son et al., 2009), and knock-in mice (Nashmi et al., 2003; Fonck et al., 2009; Xiao et al., 2009). Because the $\beta2$ subunit mutations described in this paper are in the M3–M4 loop, we used

only FP-tagged α4 subunits and avoided using our previously described M3–M4 loop FP-tagged β2 subunits.

Overcoming ER export bottleneck(s) by altering β2 subunit export/retention motifs

Electron microscopy studies in mouse dorsal raphe and rat cortical neurons show that endogenous α4β2 nAChRs localize at least partially to the smooth ER (Hill et al., 1993; Commons, 2008). Similarly, our pilot TIRFM experiments (presented in Materials and methods) showed that many—perhaps most—α4β2 nAChRs localize to the ER, but α4β4 nAChRs primarily localized to the PM (Fig. 1). Like previous authors (Ren et al., 2005; Kracun et al., 2008), we compared the β2 and β4 subunit protein sequences to identify specific motifs that mediate the ER retention of receptors (Fig. 2 D, 1). This led to construction of the enhanced ER export β4-like β2 subunit that both (a) contains an LFM ER export motif (Mancias and Goldberg, 2008) and (b) lacks an RRQR ER retention/retrieval motif (Michelsen et al., 2005). Interestingly, human β2 subunits contain the LFM ER export motif as well as the RRQR motif, whereas chicken α4β2 nAChRs contain the LFM motif but do not possess the RRQR motif (Fig. 2 D, 2). Thus, our data suggest that human and chicken receptors might exit the ER more efficiently than mouse and rat receptors, but human and chicken receptors also harbor the RRQR motif and would therefore still be up-regulated by chronic nicotine.

Nicotine and β2 subunit mutations increase the PM insertion of nAChRs

TIRFM experiments recapitulated that nicotine up-regulated PM α4β2-wt nAChRs, despite markedly increasing the proportion of ER-localized α4β2-wt nAChRs (Fig. 2, B and C). A disruption of the β2 RRQR ER retention/retrieval signal increased the proportion of nAChRs at the PM (Fig. 3 B), and alterations of LFM motifs in α4 and β2 increased the surface expression of α4β2 receptors monotonically with the number of LFM motifs present in the receptor pentamer (Fig. 4, A–D). These nicotine and double mutation effects approached a common maximum; treatment with nicotine caused only a small increase in the PM level of double-mutant β2 subunits (Fig. 2, B and C).

The control of ER exit rate

Assembled nAChRs presumably enter COPII-containing ERES. Four Sec24 isoforms (A, B, C, and D) recognize distinct ER exit codes in cargo proteins and participate in COPII vesicle assembly (Russell and Stagg, 2010). ER exit codes include LL motifs, bound by the Sec24A isoform, and I/LXM motifs, bound by Sec24D (Wendeler et al., 2007; Mancias and Goldberg, 2008). The LL ER export motifs were previously identified in the M3–M4 loop of nAChR subunits (Ren et al., 2005). In our obser-

vations with Sec24D-mcherry, the number of ERES per cell increased monotonically with the number of LFM motifs present in the receptor pentamer (Fig. 6 C). The available data thus show that α4β2 nAChRs possess ER export motifs recognizing Sec24A and Sec24D molecules. Human α4β2 pentamers possess five LFM motifs, and mouse α4β2 receptors contain two or three; possibly, nAChR ER export rates differ among species.

RXR motifs enhance the ER localization of ion channels (Scott et al., 2003; Gassmann et al., 2005). In our studies, mutation of the β2 M3–M4 loop RRQR to AAQA resulted in markedly increased ER export and membrane-localized receptors versus wt nAChRs.

The control of ERES numbers

Our observation that ERES numbers increase—even without nicotine—for enhanced ER export of nAChRs shows that the recruitment of ERES depends directly on ER export efficiency and extends previous observations that simple coexpression of membrane proteins can enhance ERES number (Farhan et al., 2008). Indeed, we found that the number of ERES per cell increased monotonically with the number of LFM motifs present in the receptor pentamer (Fig. 6 C). Reciprocally, increasing the number of LFM motifs also biased the receptors toward the $(\alpha4)_2(\beta2)_3$ stoichiometry (Fig. 5 B and Table I); possibly, these Sec24D-binding sites allow Sec24D to stabilize this stoichiometry. Thus, increasing the number of Sec24-binding sites in the nAChR protein stabilizes a pentamer that binds Sec24D, and the Sec24D-containing ERES complex is in turn stabilized by binding to nAChR pentamers. We also observed an increase in the number of ERES in cells expressing α4-eGFPβ2-365AAQA368 nAChRs. The β2-365AAQA368 mutation may increase ERES numbers by preventing the ER retention of assembled nAChRs and/or by decreasing the likelihood that COPII is displaced by a COPI-mediated ER retrieval of exported receptors.

Perhaps a therapeutic mechanism arises from the observation for wt nAChRs that the chronic nicotine–nAChR interaction also directly recruits ERES (Fig. 6 E). The nicotine–nAChR complex thus produces noticeable redistribution of at least one other ER protein, which is remarkable even if one does not consider eventual up-regulation at the PM. If the newly recruited ERES are available to other cargo proteins, this could produce enhanced ER exit of other proteins. We do not yet know to what extent the nicotine–nAChR interaction changes the overall morphology of the ER. In an alternative analysis of the TIRF data, we did find that nicotine increased the number of pixels in the ER category, as judged by α4-FP fluorescence; but additional studies are required to gauge the generality of this finding. We would like to use a marker different from the ER-Tracker Green, which also labels an ion channel.

When a previous study (Farhan et al., 2008) found that overexpression of the GAT1 transporter also induced additional ERES, the authors suggested that this induces ER stress. Our experiments go further by showing that the enhancement depends not merely on the presence of a cargo protein but also on the interaction between an intracellular ligand and a cargo protein (nicotine–nAChR). Our data are fully consistent with the view that the nicotine–nAChR interaction, by affecting ER stress levels, also changes a downstream unfolded protein response. This topic bears on possible cell-limited mechanisms for the inverse correlation between a person's history of smoking and his or her susceptibility to Parkinson's disease (Ritz et al., 2007), in addition to the previously suggested circuit-based mechanism (Nashmi et al., 2007; Xiao et al., 2009). The present methods could serve in high-content drug screening.

The control of nAChR stoichiometry

This study reveals two processes within the ER and TG/TGN that bias the α4β2 nAChR population toward the $(\alpha 4)_2 (\beta 2)_3$ stoichiometry. First, our NFRET experiments showed that wt α4β2 receptors assemble with a roughly equal proportion of $(\alpha 4)_2 (\beta 2)_3$ and $(\alpha 4)_3 (\beta 2)_2$ stoichiometries in the ER, and that both stoichiometries traffic to the trans-Golgi (Fig. 5 B). Nicotine treatment of wt α4β2-expressing cells increased the assembly of $(\alpha 4)_2 (\beta 2)_3$ nAChRs (Fig. 5 B and Table I). We know that nicotine-induced changes in nAChR stoichiometry are initiated in the ER, because in nicotine-treated cells, the TG/TGN contained mostly $(\alpha 4)_2 (\beta 2)_3$ receptors (Fig. 5 B and Table I). These data correspond with previous results based on glycosylation and molecular weight measures, showing that up-regulation is initiated in the ER (Nelson et al., 2003; Kuryatov et al., 2005; Sallette et al., 2005). The thermodynamic driving force for this stoichiometry shift is presumably the tighter binding of nicotine to the $(\alpha 4)_2 (\beta 2)_3$ stoichiometry (Nelson et al., 2003). Second, in contrast to wt receptors, mutant β2-L349M and β2-365AAQA368 subunits preferentially assembled nAChRs with $(\alpha 4)_2 (\beta 2)_3$ stoichiometry (Fig. 5 B and Table I). We suggested above that this effect also arises from a binding–stabilization mechanism between
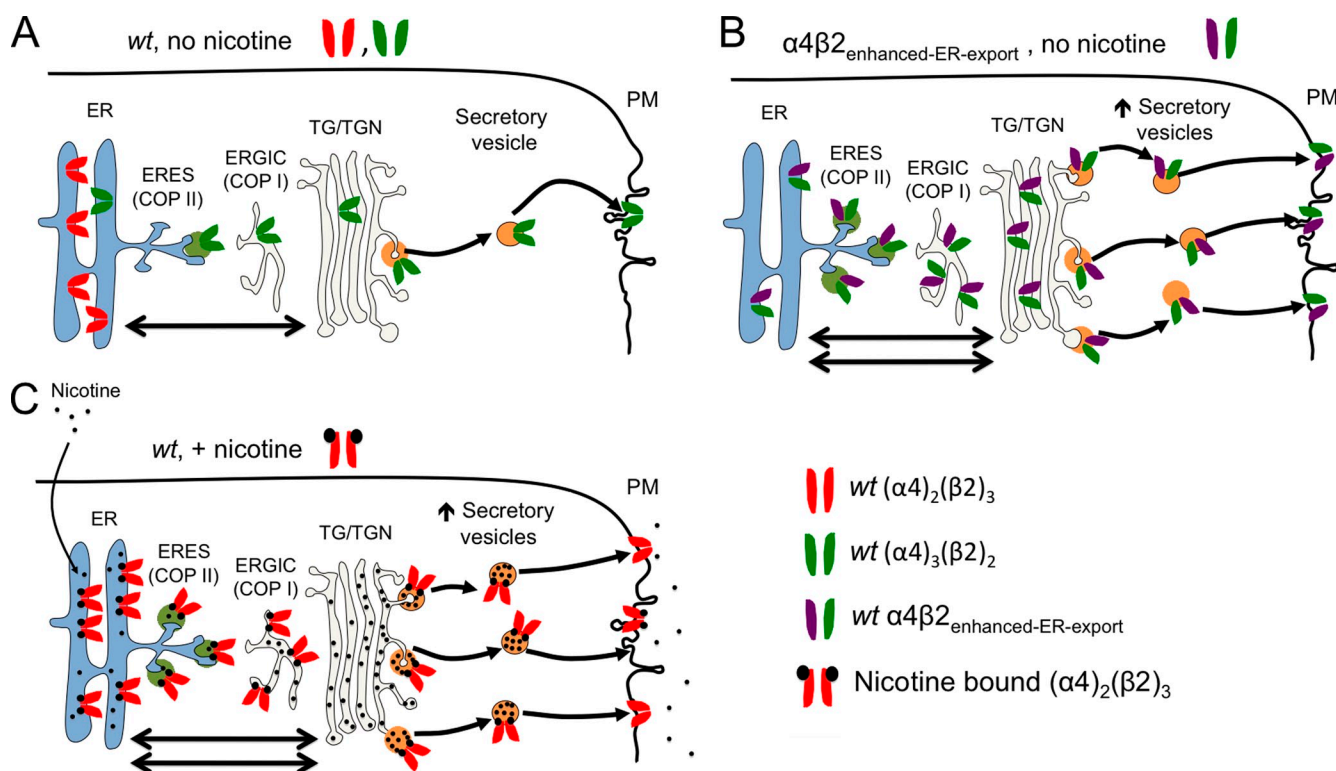
Figure 8. A more detailed view of subcellular components in nAChR up-regulation, complementing the schematic view of Fig. 7. ER, COPII vesicles, Golgi apparatus, secretory vesicles, PM, and nicotine are shown. Four types of α4β2 nAChRs are defined in the box. (A) wt nAChRs assemble in the ER and exit via COPII-containing ERES. Vesicles bud from the TG/TGN and transport receptors to the PM. (B) α4β2$_{enhanced-ER-export}$ nAChRs show increased ER exit and therefore eventually reach the PM in greater numbers. (C) Nicotine is now present at extracellular concentrations produced by smoking (0.1–1 µM). Nicotine enters the ER and stabilizes nAChRs with $(\alpha 4)_2 (\beta 2)_3$ stoichiometry (see Fig. 7; step 8). Newly assembled nicotine-bound nAChRs show increased ER exit; therefore, greater numbers of nAChRs undergo anterograde trafficking and insertion into the PM. Nicotine concentrations are elevated within ERGIC, TG/TGN, and secretory vesicles via acid trapping (Lester et al., 2009). At the PM, smoking-relevant nicotine concentrations only partially occupy nAChRs, revealing enhanced function of up-regulated α4β2 nAChRs.

nAChRs and Sec24 proteins rather than between nAChRs and nicotine.

Insights from the SePhaChARNS 2.0 model

The SePhaChARNS 2.0 model formalizes the notion that some effects of chronic nicotine have a cell-delimited basis, analyzable in terms of molecular states and subcellular compartments. Although SePhaChARNS 2.0 suggests that nicotine pharmacologically chaperones a "fully folded" state (Kuryatov et al., 2005; Lester et al., 2009), the formalism is fully compatible with previous statements that the nicotine-favored state(s) matures more easily (Sallette et al., 2005), has a distinct phosphorylation pattern (Pollock et al., 2009), has a distinct, stabilized conformation (Harkness and Millar, 2002; Vallejo et al., 2005), or is less susceptible to proteasome-mediated degradation (Rezvani et al., 2007). The key common concept is that the nicotine-favored state is both more capable of export and less susceptible to misfolding/degradation than other states within the ER.

Future versions of the SePhaChARNS model should more fully incorporate the effects on subunit stoichiometry. To simulate how enhanced ER export β2 subunits increase ERES numbers, one should also incorporate the idea that these subunits bias the cell toward assembled ERES as well as the extension that this interaction stabilizes ERES proteins themselves against degradation. Future experiments should incorporate time-resolved measurements to test and to refine the kinetic values. Time-resolved experiments must also account for the maturation of the FPs, which typically requires 10^3–10^4 s. At present, however, the model satisfactorily accounts for the following ideas: (a) chaperoning by nicotine precedes export from the ER; (b) nicotine enhances an endogenous process by a factor of 10–30; (c) for wt nAChRs, up-regulation at the PM appears to be limited by ER export; and (d) up-regulation does not depend on flux limitations beyond ER export. Thus, even at this early stage, the SePhaChARNS model allows one to advance beyond purely verbal descriptions of interrelated mechanisms.

Conclusions

The present subcellularly resolved imaging data agree with the views that the mechanisms of α4β2 nAChR trafficking depend on the balance between ER export and retention/retrieval motifs in α4β2 pentamers; that this balance depends in part on the stoichiometry of α4β2 nAChRs; that trafficking and stoichiometry influence each other; and that a sustained interaction between nicotine and nAChRs exerts control over both processes. Chief findings are summarized in Fig. 8. wt $(\alpha4)_3(\beta2)_2$ receptors contain a 3:2 ratio of LFM (ER export motifs) to RRQR (ER retention/retrieval) motifs and traffic efficiently to the PM, whereas $(\alpha4)_2(\beta2)_3$ nAChRs with a 2:3 ratio of ER export to retention/retrieval motifs

largely localize to the ER. Enhanced ER export mutant β2 subunits alter this balance in favor of PM localization. Our experiments also show that an overall increase of PM α4β2 nAChRs results from the stabilization of assembled receptors by nicotine.

Despite the generality of nicotine-induced up-regulation (see Introduction), nicotine-induced up-regulation also displays selectivity at every level thus far examined (Nguyen et al., 2003; Perry et al., 2007; Doura et al., 2008; Lester et al., 2009; Xiao et al., 2009). These "tiers of selectivity" include major brain regions (Pauly et al., 1991; Marks et al., 1992) and neuronal cell types (Nashmi et al., 2007; Xiao et al., 2009). At the level of individual neurons, up-regulation is selective between compartments: somatodendritic versus axon terminal (Xiao et al., 2009). At the level of classical pharmacology, up-regulation displays selectivity among binding subtypes, emphasizing high-affinity nAChRs such as α4β2. At the level of functional states, some up-regulated receptors are primarily activated by acute nicotine, whereas others are primarily desensitized (Xiao et al., 2009). At the level of the α4β2* subtype, up-regulation displays selectivity among the subunits that occupy the fifth "auxiliary" position (Kuryatov et al., 2008). Good candidates for mechanisms that govern this specificity include the expression of additional nAChR subunits and auxiliary proteins such as lynx, based on the observed expression of these additional genes (Lester et al., 2009). The present study shows how to use a favorable clonal line, good optics, and a quantitative model to analyze the effects of expressing these additional molecules.

REFERENCES

Abramoff, M.D., P. Magelhaes, and S.J. Ram. 2004. Image processing with ImageJ. *Biophotonics International*. 11:36–42.

Albuquerque, E.X., E.F. Pereira, M. Alkondon, and S.W. Rogers. 2009. Mammalian nicotinic acetylcholine receptors: from structure to function. *Physiol. Rev.* 89:73–120. doi:10.1152/physrev.00015.2008

Breese, C.R., M.J. Marks, J. Logel, C.E. Adams, B. Sullivan, A.C. Collins, and S. Leonard. 1997. Effect of smoking history on [³H]nicotine binding in human postmortem brain. *J. Pharmacol. Exp. Ther.* 282:7–13.

Brock, C., L. Boudier, D. Maurel, J. Blahos, and J.P. Pin. 2005. Assembly-dependent surface targeting of the heterodimeric GABA_B receptor is controlled by COPI but not 14-3-3. *Mol. Biol. Cell.* 16:5572–5578. doi:10.1091/mbc.E05-05-0400

Buisson, B., and D. Bertrand. 2001. Chronic exposure to nicotine upregulates the human (α)4((β)2 nicotinic acetylcholine receptor function. *J. Neurosci.* 21:1819–1829.

Cole, N.B., C.L. Smith, N. Sciaky, M. Terasaki, M. Edidin, and J. Lippincott-Schwartz. 1996. Diffusional mobility of Golgi proteins in membranes of living cells. *Science.* 273:797–801. doi:10.1126/science.273.5276.797

Commons, K.G. 2008. α4 containing nicotinic receptors are positioned to mediate postsynaptic effects on 5-HT neurons in the rat dorsal raphe nucleus. *Neuroscience.* 153:851–859. doi:10.1016/j.neuroscience.2008.02.056

Court, J.A., S. Lloyd, N. Thomas, M.A. Piggott, E.F. Marshall, C.M. Morris, H. Lamb, R.H. Perry, M. Johnson, and E.K. Perry. 1998. Dopamine and nicotinic receptor binding and the levels of dopamine and homovanillic acid in human brain related to tobacco use. *Neuroscience.* 87:63–78. doi:10.1016/S0306-4522(98)00088-8

Darsow, T., T.K. Booker, J.C. Piña-Crespo, and S.F. Heinemann. 2005. Exocytic trafficking is required for nicotine-induced up-regulation of α 4 β 2 nicotinic acetylcholine receptors. *J. Biol. Chem.* 280:18311–18320. doi:10.1074/jbc.M501157200

Doura, M.B., A.B. Gold, A.B. Keller, and D.C. Perry. 2008. Adult and periadolescent rats differ in expression of nicotinic cholinergic receptor subtypes and in the response of these subtypes to chronic nicotine exposure. *Brain Res.* 1215:40–52. doi:10.1016/j.brainres.2008.03.056

Drenan, R.M., R. Nashmi, P. Imoukhuede, H. Just, S. McKinney, and H.A. Lester. 2008. Subcellular trafficking, pentameric assembly, and subunit stoichiometry of neuronal nicotinic acetylcholine receptors containing fluorescently labeled α6 and β3 subunits. *Mol. Pharmacol.* 73:27–41. doi:10.1124/mol.107.039180

Farhan, H., M. Weiss, K. Tani, R.J. Kaufman, and H.P. Hauri. 2008. Adaptation of endoplasmic reticulum exit sites to acute and chronic increases in cargo load. *EMBO J.* 27:2043–2054. doi:10.1038/emboj.2008.136

Feige, J.N., D. Sage, W. Wahli, B. Desvergne, and L. Gelman. 2005. PixFRET, an ImageJ plug-in for FRET calculation that can accommodate variations in spectral bleed-throughs. *Microsc. Res. Tech.* 68:51–58. doi:10.1002/jemt.20215

Fenster, C.P., T.L. Whitworth, E.B. Sheffield, M.W. Quick, and R.A. Lester. 1999. Upregulation of surface α4β2 nicotinic receptors is initiated by receptor desensitization after chronic exposure to nicotine. *J. Neurosci.* 19:4804–4814.

Fish, K.N. 2009. Total internal reflection fluorescence (TIRF) microscopy. *Curr. Protoc. Cytom.* 50:12.18.1–12.18.13.

Fonck, C., R. Nashmi, R. Salas, C. Zhou, Q. Huang, M. De Biasi, R.A. Lester, and H.A. Lester. 2009. Demonstration of functional α4-containing nicotinic receptors in the medial habenula. *Neuropharmacology.* 56:247–253. doi:10.1016/j.neuropharm.2008.08.021

Fu, X.W., J. Lindstrom, and E.R. Spindel. 2009. Nicotine activates and up-regulates nicotinic acetylcholine receptors in bronchial epithelial cells. *Am. J. Respir. Cell Mol. Biol.* 41:93–99. doi:10.1165/rcmb.2008-0352OC

Gassmann, M., C. Haller, Y. Stoll, S.A. Aziz, B. Biermann, J. Mosbacher, K. Kaupmann, and B. Bettler. 2005. The RXR-type endoplasmic reticulum-retention/retrieval signal of GABA$_{B1}$ requires distant spacing from the membrane to function. *Mol. Pharmacol.* 68:137–144.

Gopalakrishnan, M., L.M. Monteggia, D.J. Anderson, E.J. Molinari, M. Piattoni-Kaplan, D. Donnelly-Roberts, S.P. Arneric, and J.P. Sullivan. 1996. Stable expression, pharmacologic properties and regulation of the human neuronal nicotinic acetylcholine α 4 β 2 receptor. *J. Pharmacol. Exp. Ther.* 276:289–297.

Gotti, C., M. Zoli, and F. Clementi. 2006. Brain nicotinic acetylcholine receptors: native subtypes and their relevance. *Trends Pharmacol. Sci.* 27:482–491. doi:10.1016/j.tips.2006.07.004

Harkness, P.C., and N.S. Millar. 2002. Changes in conformation and subcellular distribution of α4β2 nicotinic acetylcholine receptors revealed by chronic nicotine treatment and expression of subunit chimeras. *J. Neurosci.* 22:10172–10181.

Heinzer, S., S. Wörz, C. Kalla, K. Rohr, and M. Weiss. 2008. A model for the self-organization of exit sites in the endoplasmic reticulum. *J. Cell Sci.* 121:55–64. doi:10.1242/jcs.013383

Hill, J.A. Jr., M. Zoli, J.P. Bourgeois, and J.P. Changeux. 1993. Immunocytochemical localization of a neuronal nicotinic receptor: the β 2-subunit. *J. Neurosci.* 13:1551–1568.

Imoukhuede, P.I., F.J. Moss, D.J. Michael, R.H. Chow, and H.A. Lester. 2009. Ezrin mediates tethering of the γ-aminobutyric acid transporter GAT1 to actin filaments via a C-terminal PDZ-interacting domain. *Biophys. J.* 96:2949–2960. doi:10.1016/j.bpj.2008.11.070

Kalivas, P.W., R.T. Lalumiere, L. Knackstedt, and H. Shen. 2009. Glutamate transmission in addiction. *Neuropharmacology.* 56:169–173. doi:10.1016/j.neuropharm.2008.07.011

Kauer, J.A., and R.C. Malenka. 2007. Synaptic plasticity and addiction. *Nat. Rev. Neurosci.* 8:844–858. doi:10.1038/nrn2234

Ke, L., C.M. Eisenhour, M. Bencherif, and R.J. Lukas. 1998. Effects of chronic nicotine treatment on expression of diverse nicotinic acetylcholine receptor subtypes. I. Dose- and time-dependent effects of nicotine treatment. *J. Pharmacol. Exp. Ther.* 286:825–840.

Khiroug, S.S., E. Pryazhnikov, S.K. Coleman, A. Jeromin, K. Keinänen, and L. Khiroug. 2009. Dynamic visualization of membrane-inserted fraction of pHluorin-tagged channels using repetitive acidification technique. *BMC Neurosci.* 10:141. doi:10.1186/1471-2202-10-141

Kishi, M., and J.H. Steinbach. 2006. Role of the agonist binding site in up-regulation of neuronal nicotinic α4β2 receptors. *Mol. Pharmacol.* 70:2037–2044. doi:10.1124/mol.106.029298

Koob, G.F. 2009. New dimensions in human laboratory models of addiction. *Addict. Biol.* 14:1–8. doi:10.1111/j.1369-1600.2008.00127.x

Kracun, S., P.C. Harkness, A.J. Gibb, and N.S. Millar. 2008. Influence of the M3-M4 intracellular domain upon nicotinic acetylcholine receptor assembly, targeting and function. *Br. J. Pharmacol.* 153:1474–1484. doi:10.1038/sj.bjp.0707676

Kuryatov, A., J. Luo, J. Cooper, and J. Lindstrom. 2005. Nicotine acts as a pharmacological chaperone to up-regulate human α4β2 acetylcholine receptors. *Mol. Pharmacol.* 68:1839–1851.

Kuryatov, A., J. Onksen, and J. Lindstrom. 2008. Roles of accessory subunits in α4β2* nicotinic receptors. *Mol. Pharmacol.* 74:132–143. doi:10.1124/mol.108.046789

Lester, H.A., C. Xiao, R. Srinivasan, C.D. Son, J. Miwa, R. Pantoja, M.R. Banghart, D.A. Dougherty, A.M. Goate, and J.C. Wang. 2009. Nicotine is a selective pharmacological chaperone of acetylcholine receptor number and stoichiometry. Implications for drug discovery. *AAPS J.* 11:167–177. doi:10.1208/s12248-009-9090-7

Mancias, J.D., and J. Goldberg. 2008. Structural basis of cargo membrane protein discrimination by the human COPII coat machinery. *EMBO J.* 27:2918–2928. doi:10.1038/emboj.2008.208

Marks, M.J., J.B. Burch, and A.C. Collins. 1983. Effects of chronic nicotine infusion on tolerance development and nicotinic receptors. *J. Pharmacol. Exp. Ther.* 226:817–825.

Marks, M.J., J.A. Stitzel, and A.C. Collins. 1985. Time course study of the effects of chronic nicotine infusion on drug response and brain receptors. *J. Pharmacol. Exp. Ther.* 235:619–628.

Marks, M.J., J.R. Pauly, S.D. Gross, E.S. Deneris, I. Hermans-Borgmeyer, S.F. Heinemann, and A.C. Collins. 1992. Nicotine binding and nicotinic receptor subunit RNA after chronic nicotine treatment. *J. Neurosci.* 12:2765–2784.

Matta, S.G., D.J. Balfour, N.L. Benowitz, R.T. Boyd, J.J. Buccafusco, A.R. Caggiula, C.R. Craig, A.C. Collins, M.I. Damaj, E.C. Donny, et al. 2007. Guidelines on nicotine dose selection for in vivo research. *Psychopharmacology (Berl.).* 190:269–319. doi:10.1007/s00213-006-0441-0

Michelsen, K., H. Yuan, and B. Schwappach. 2005. Hide and run. Arginine-based endoplasmic-reticulum-sorting motifs in the assembly of heteromultimeric membrane proteins. *EMBO Rep.* 6:717–722. doi:10.1038/sj.embor.7400480

Moss, F.J., P.I. Imoukhuede, K. Scott, J. Hu, J.L. Jankowsky, M.W. Quick, and H.A. Lester. 2009. GABA transporter function, oligomerization state, and anchoring: correlates with subcellularly resolved FRET. *J. Gen. Physiol.* 134:489–521. doi:10.1085/jgp.200910314

Mukhin, A.G., A.S. Kimes, S.I. Chefer, J.A. Matochik, C.S. Contoreggi, A.G. Horti, D.B. Vaupel, O. Pavlova, and E.A. Stein. 2008. Greater nicotinic acetylcholine receptor density in smokers than in nonsmokers: a PET study with 2-18F-FA-85380. *J. Nucl. Med.* 49:1628–1635. doi:10.2967/jnumed.108.050716

Nashmi, R., M.E. Dickinson, S. McKinney, M. Jareb, C. Labarca, S.E. Fraser, and H.A. Lester. 2003. Assembly of α4β2 nicotinic acetylcholine receptors assessed with functional fluorescently labeled subunits: effects of localization, trafficking, and nicotine-induced upregulation in clonal mammalian cells and in cultured midbrain neurons. *J. Neurosci.* 23:11554–11567.

Nashmi, R., C. Xiao, P. Deshpande, S. McKinney, S.R. Grady, P. Whiteaker, Q. Huang, T. McClure-Begley, J.M. Lindstrom, C. Labarca, et al. 2007. Chronic nicotine cell specifically upregulates functional α4* nicotinic receptors: basis for both tolerance in midbrain and enhanced long-term potentiation in perforant path. *J. Neurosci.* 27:8202–8218. doi:10.1523/JNEUROSCI.2199-07.2007

Nelson, M.E., A. Kuryatov, C.H. Choi, Y. Zhou, and J. Lindstrom. 2003. Alternate stoichiometries of α4β2 nicotinic acetylcholine receptors. *Mol. Pharmacol.* 63:332–341. doi:10.1124/mol.63.2.332

Nguyen, H.N., B.A. Rasmussen, and D.C. Perry. 2003. Subtype-selective up-regulation by chronic nicotine of high-affinity nicotinic receptors in rat brain demonstrated by receptor autoradiography. *J. Pharmacol. Exp. Ther.* 307:1090–1097. doi:10.1124/jpet.103.056408

Oancea, E., J.T. Wolfe, and D.E. Clapham. 2006. Functional TRPM7 channels accumulate at the plasma membrane in response to fluid flow. *Circ. Res.* 98:245–253. doi:10.1161/01.RES.0000200179.29375.cc

Pauly, J.R., M.J. Marks, S.D. Gross, and A.C. Collins. 1991. An autoradiographic analysis of cholinergic receptors in mouse brain after chronic nicotine treatment. *J. Pharmacol. Exp. Ther.* 258:1127–1136.

Peng, X., V. Gerzanich, R. Anand, P.J. Whiting, and J. Lindstrom. 1994. Nicotine-induced increase in neuronal nicotinic receptors results from a decrease in the rate of receptor turnover. *Mol. Pharmacol.* 46:523–530.

Perry, D.C., D. Mao, A.B. Gold, J.M. McIntosh, J.C. Pezzullo, and K.J. Kellar. 2007. Chronic nicotine differentially regulates α6- and β3-containing nicotinic cholinergic receptors in rat brain. *J. Pharmacol. Exp. Ther.* 322:306–315. doi:10.1124/jpet.107.121228

Pollock, V.V., T. Pastoor, C. Katnik, J. Cuevas, and L. Wecker. 2009. Cyclic AMP-dependent protein kinase A and protein kinase C phosphorylate α4β2 nicotinic receptor subunits at distinct stages of receptor formation and maturation. *Neuroscience.* 158:1311–1325. doi:10.1016/j.neuroscience.2008.11.032

Ren, X.Q., S.B. Cheng, M.W. Treuil, J. Mukherjee, J. Rao, K.H. Braunewell, J.M. Lindstrom, and R. Anand. 2005. Structural determinants of α4β2 nicotinic acetylcholine receptor trafficking. *J. Neurosci.* 25:6676–6686. doi:10.1523/JNEUROSCI.1079-05.2005

Rezvani, K., Y. Teng, D. Shim, and M. De Biasi. 2007. Nicotine regulates multiple synaptic proteins by inhibiting proteasomal activity. *J. Neurosci.* 27:10508–10519. doi:10.1523/JNEUROSCI.3353-07.2007

Ritz, B., A. Ascherio, H. Checkoway, K.S. Marder, L.M. Nelson, W.A. Rocca, G.W. Ross, D. Strickland, S.K. Van Den Eeden, and J. Gorell. 2007. Pooled analysis of tobacco use and risk of Parkinson disease. *Arch. Neurol.* 64:990–997. doi:10.1001/archneur.64.7.990

Russell, C., and S.M. Stagg. 2010. New insights into the structural mechanisms of the COPII coat. *Traffic.* 11:303–310. doi:10.1111/j.1600-0854.2009.01026.x

Sallette, J., S. Pons, A. Devillers-Thiery, M. Soudant, L. Prado de Carvalho, J.P. Changeux, and P.J. Corringer. 2005. Nicotine up-regulates its own receptors through enhanced intracellular maturation. *Neuron.* 46:595–607. doi:10.1016/j.neuron.2005.03.029

Schaub, B.E., B. Berger, E.G. Berger, and J. Rohrer. 2006. Transition of galactosyltransferase 1 from trans-Golgi cisterna to the trans-Golgi network is signal mediated. *Mol. Biol. Cell.* 17:5153–5162. doi:10.1091/mbc.E06-08-0665

Schwartz, R.D., and K.J. Kellar. 1983. Nicotinic cholinergic receptor binding sites in the brain: regulation in vivo. *Science.* 220:214–216. doi:10.1126/science.6828889

Scott, D.B., T.A. Blanpied, G.T. Swanson, C. Zhang, and M.D. Ehlers. 2001. An NMDA receptor ER retention signal regulated by phosphorylation and alternative splicing. *J. Neurosci.* 21:3063–3072.

Scott, D.B., T.A. Blanpied, and M.D. Ehlers. 2003. Coordinated PKA and PKC phosphorylation suppresses RXR-mediated ER retention and regulates the surface delivery of NMDA receptors. *Neuropharmacology.* 45:755–767. doi:10.1016/S0028-3908(03)00250-8

Slimko, E.M., S. McKinney, D.J. Anderson, N. Davidson, and H.A. Lester. 2002. Selective electrical silencing of mammalian neurons in vitro by the use of invertebrate ligand-gated chloride channels. *J. Neurosci.* 22:7373–7379.

Son, C.D., F.J. Moss, B.N. Cohen, and H.A. Lester. 2009. Nicotine normalizes intracellular subunit stoichiometry of nicotinic receptors carrying mutations linked to autosomal dominant nocturnal frontal lobe epilepsy. *Mol. Pharmacol.* 75:1137–1148. doi:10.1124/mol.108.054494

Staley, J.K., S. Krishnan-Sarin, K.P. Cosgrove, E. Krantzler, E. Frohlich, E. Perry, J.A. Dubin, K. Estok, E. Brenner, R.M. Baldwin, et al. 2006. Human tobacco smokers in early abstinence have higher levels of β2* nicotinic acetylcholine receptors than nonsmokers. *J. Neurosci.* 26:8707–8714. doi:10.1523/JNEUROSCI.0546-06.2006

Stephens, D.J., N. Lin-Marq, A. Pagano, R. Pepperkok, and J.P. Paccaud. 2000. COPI-coated ER-to-Golgi transport complexes segregate from COPII in close proximity to ER exit sites. *J. Cell Sci.* 113:2177–2185.

Vallejo, Y.F., B. Buisson, D. Bertrand, and W.N. Green. 2005. Chronic nicotine exposure upregulates nicotinic receptors by a novel mechanism. *J. Neurosci.* 25:5563–5572. doi:10.1523/JNEUROSCI.5240-04.2005

Wendeler, M.W., J.P. Paccaud, and H.P. Hauri. 2007. Role of Sec24 isoforms in selective export of membrane proteins from the endoplasmic reticulum. *EMBO Rep.* 8:258–264. doi:10.1038/sj.embor.7400893

Whiteaker, P., C.G. Sharples, and S. Wonnacott. 1998. Agonist-induced up-regulation of α4β2 nicotinic acetylcholine receptors in M10 cells: pharmacological and spatial definition. *Mol. Pharmacol.* 53:950–962.

Wiseman, R.L., E.T. Powers, J.N. Buxbaum, J.W. Kelly, and W.E. Balch. 2007. An adaptable standard for protein export from the endoplasmic reticulum. *Cell.* 131:809–821. doi:10.1016/j.cell.2007.10.025

Xiao, C., R. Nashmi, S. McKinney, H. Cai, J.M. McIntosh, and H.A. Lester. 2009. Chronic nicotine selectively enhances α4β2* nicotinic acetylcholine receptors in the nigrostriatal dopamine pathway. *J. Neurosci.* 29:12428–12439. doi:10.1523/JNEUROSCI.2939-09.2009